PHYSICAL REVIEW A **110**, 022611 (2024)

Critical properties of quantum Fisher information of SU(1,1)-dynamic systems

Yuyang Tang,[1,*] Yu Yang,[1,*] Min An,[1] Jikun Xie,[1] Yunlong Wang,[1] Feiran Wang,[1,2] and Fuli Li[1,†]
[1] *Ministry of Education Key Laboratory for Nonequilibrium Synthesis and Modulation of Condensed Matter, Shaanxi Province Key Laboratory of Quantum Information and Quantum Optoelectronic Devices, School of Physics, Xi'an Jiaotong University, Xi'an 710049, China*
[2] *School of Science, Xi'an Polytechnic University, Xi'an 710048, China*

(Received 8 May 2024; accepted 31 July 2024; published 13 August 2024)

Quantum Fisher information (QFI) may exhibit the irregular behavior at the critical point of phase transitions of a physical system and be very sensitive to slight variations of some controlling parameters. This parameter sensitivity may be used for quantum parameter estimation or quantum sensing. In this study, taking the quantum Rabi model as an example, we investigate the critical properties of the QFI for the parameter estimation at the critical point of the SU(1,1) dynamic systems. We show that the QFI goes divergently in the sixth power law (T^6) of the parameter coding time around the critical point. After taking into the consumption of energy during the dynamic evolution, we find that the variation of the QFI around the critical point is scaled by the Heisenberg scaling T^2. It is noticed that for nonclassical initial probe states the scaling of QFI can beat the standard quantum limit (n_0) as a function of the initial mean phonon number n_0. The homodyne and phonon-number measurement schemes are compared. We find that the quantum Cramér-Rao bound can be reached by use of the phonon-number detection scheme. However, it is more sensitive to the noise than the homodyne detection scheme. We extend the investigation to a two-mode non-Hermitian system and show that the QFI exhibits the same irregular properties at the exceptional point, revealing that for the SU(1,1) dynamic systems the QFI universally diverges as T^6 at the critical point.

DOI: 10.1103/PhysRevA.110.022611

I. INTRODUCTION

Quantum sensing refers to the utilization of quantum resources for estimating parameters [1]. In past years, many methods have been proposed to enhance the precision of quantum sensing, from seeking optimal initial states (optimal measurement operators), to operating quantum control [2–5], to exploiting quantum uncertainty causality orders [6,7]. Recently, it has been discovered that critical properties of physical systems also constitute a metrological resource, since a slight variation in the parameter can manifest a significant change in the observable quantity, thereby enhancing the precision of sensing [8–11]. So far, there are several approaches to achieve quantum critical sensing, including constructing non-Hermitian systems [12–14], as well as leveraging topological and dynamical phase transitions [15–18].

Quantum phase transitions (QPTs) are characterized by significant variation in the observables of a system subjected to infinitesimal variations of a control parameter. These differences manifest as substantial structural alterations in the state of the system (i.e., the change of ground state) [19]. Many physical models can be used for quantum phase transition critical sensing, such as the Dicke model, the Lipkin-Meshkov-Glick (LMG) model, and the quantum Rabi model (QRM). The QRM plays an important role in quantum optics, comprising a two-level system coupled with a bosonic field mode, which undergoes a superradiant QPT at the critical point [20]. Recent studies have revealed that it can lead to enhanced sensing capabilities near the critical point by preparing the initial state in the ground state and employing adiabatic evolution [21]. However, it is proved that it cannot reach the Heisenberg limit (HL) with the requirement of adiabatic condition [22]. To address this problem, a dynamic method without the adiabatic ground state preparation was proposed [23], and it has been demonstrated to be efficient in numerous physical systems [24,25].

There are still some problems about modulating a QRM system to its critical point for the instability originating from QPT. The ion trap can serve as an excellent platform due to its stability and ease of manipulation [26]. The system play a crucial role in various physical applications, such as quantum simulation [27–29], quantum state preparation [30,31], and quantum metrology [32]. In recent years, researchers have discovered the potential of utilizing ion trap systems for quantum sensing, achieving precision beyond the standard quantum limit [33,34].

In this work we consider the ion trap system while the sideband resonance Hamiltonian is transformed into the QRM in the Lamb-Dicke regime, and is then represented as an canonical form in term of the time-independent SU(1,1) algebra. For this SU(1,1) coding dynamics system, the QPT occurs when $\tilde{g} = 1$ is satisfied (see Sec. II). We find that after the total evolution time T, the QFI of $\tilde{g}$ exhibits a significantly growth with the scaling law of T^6 at the critical point. The estimation precision of $\tilde{g}$ with probe states such as coherent state, Fock number state, and a linear superposition of number states can reach the Heisenberg scaling $\sim\langle\hat{N}^2\rangle T^2$, where $\langle\hat{N}\rangle$

---

[*] These authors contributed equally to this work.

[†] Contact author: flli@xjtu.edu.cn

represents the average phonon number. However, only the nonclassical states such as Fock number state and a linear superposition of number states can surpass the standard quantum limit (SQL) with the same initial phonon number n_0. Two measurement schemes are also investigated, homodyne detection (HD) and average phonon number detection (APND), and APND is proved to be better for its attainabilities of the quantum Cramér-Rao bound (QCRB). We also demonstrate that with finite noise the critical enhanced sensing can still be maintained. Furthermore, the two-mode non-Hermitian model following the SU(1,1) symmetry is also discussed, which gives the same scaling law of T^6 in the QFI.

The remainder of this paper is organized as follows. Section II introduces the Hamiltonian of ion trap system in the rotation frame. With the help of SU(1,1) algebra, we compute the QFI of parameter in Sec. III. Then we discuss the limits of the estimation in Sec. IV based on different initial states. In Sec. V we investigate the precision of measurements by HD and APND in the scenario of absence of dissipation and presence of dissipation, separately. In Sec. VI the extension of a two-mode non-Hermitian model is explored. Finally, we give a conclusion in Sec. VII.

II. MODEL

The quantum dynamics of a single two-level ion trapped in the Paul trap and driven by a light field is described by [26,29,35,36]

$$\hat{H} = \hbar\omega_r\hat{a}^\dagger\hat{a} + \tfrac{1}{2}\hbar\omega_q\hat{\sigma}_z + \hbar\Omega_0(\hat{\sigma}_+ + \hat{\sigma}_-)\cos(k\hat{x} - \omega_l t + \phi), \tag{1}$$

where $\hat{a}(\hat{a}^\dagger)$ is the annihilation (creation) operator of phonon for the center-mass motion of the ion, and ω_r is the frequency of phonon. The internal structure of the ion can be approximated by a two-level system with ω_q the energy difference between two internal states, and $\hat{\sigma}_{x,y,z}$ represent the Pauli matrices. The third term of (1) represents the interaction between the trapped ion and the applied light field, and $\hat{\sigma}_\pm = 1/2(\hat{\sigma}_x \pm i\hat{\sigma}_y)$. Ω_0 is the Rabi frequency with the applied light field of frequency ω_l, k the wave vector, and $\hat{x} = 1/\sqrt{2m\omega_r}(\hat{a} + \hat{a}^\dagger)$ the position operator of the center mass of the ion.

For simplification, $\phi = 0$ and $\hbar = 1$ are set in the following discussion. When the extension of wave function of the ion is much smaller than $1/k$, known as the Lamb-Dicke regime $\eta\sqrt{\langle(\hat{a} + \hat{a}^\dagger)^2\rangle} \ll 1$ [26], the Hamiltonian (1) can be approximated in the interaction picture to

$$\hat{H}_{LD} = \frac{\hbar}{2}\Omega_0\hat{\sigma}_+[1 + i\eta(\hat{a}e^{-i\omega_r t} + \hat{a}^\dagger e^{i\omega_r t})]e^{-i\delta t} + \text{H.c.}, \tag{2}$$

with the Lamb-Dicke parameter

$$\eta = kx_0, \tag{3}$$

where $x_0 = 1/\sqrt{2m\omega_r}$ is a spatial extension of the ground state wave function of a harmonic oscillator, m is the ion mass, and $\delta = \omega_l - \omega_q$.

When two laser beams of frequencies $\omega_{l,r/l,b} = \omega_q - / + \omega_r$ with the same Rabi frequency Ω_0 drive the red and blue sidebands of the ion, respectively, the Hamiltonian (1) can be changed in the rotating wave approximation to [35–38]

$$\hat{H}_{\text{QRM}} = \omega_r\hat{a}^\dagger\hat{a} + \frac{\omega_q}{2}\hat{\sigma}_z + g(\hat{\sigma}_+ + \hat{\sigma}_-)(\hat{a} + \hat{a}^\dagger), \tag{4}$$

with

$$g = \eta\Omega_0/2 \tag{5}$$

being the coupling strength between the external motion and the internal state transition of the trapped ion. When $\omega_q \gg \omega_r$, the excitation of the internal state is very weak and the ion is almost kept in the spin-down state. Therefore, the internal state can adiabatically be removed by the Schrieffer-Wolff (SW) transformation (see Appendix A) and the Hamiltonian (4) is approximated to

$$\hat{H}_{np,\tilde{g}\leqslant 1} = \omega_r\hat{a}^\dagger\hat{a} - \frac{\omega_q}{2} - \frac{\omega_r\tilde{g}^2}{4}(\hat{a}^\dagger + \hat{a})^2, \tag{6}$$

with the modified coupling strength

$$\tilde{g} = 2g/\sqrt{\omega_r\omega_q}, \tag{7}$$

where the subscript "np" refers to the normal phase, and Eq. (6) works only for $\tilde{g} \leqslant 1$. This system undergoes a normal-to-superradiant phase transition when $\tilde{g}$ approaches the critical point $\tilde{g}_c = 1$. The ground state changes abruptly, accompanying the huge increase of phonons [39]. The counterpart of (6) for $\tilde{g} > 1$ reads

$$\hat{H}_{sp,\tilde{g}>1} = \omega_r\hat{a}^\dagger\hat{a} - \frac{\omega_q}{4}(\tilde{g}^2 + \tilde{g}^{-2}) - \frac{\omega_r}{4\tilde{g}^4}(\hat{a}^\dagger + \hat{a})^2, \tag{8}$$

where the subscript "sp" represents the superdiant phase.

By virtue of SU(1,1) algebra [40], Eq. (6) can be rewritten as

$$\begin{aligned}\hat{H}_{np,\tilde{g}\leqslant 1} = {} & (-\omega_r\tilde{g}^2 + 2\omega_r)\hat{K}_0 - \frac{\omega_r\tilde{g}^2}{2}(\hat{K}_+ + \hat{K}_-) \\ & - \frac{\omega_q + \omega_r}{2},\end{aligned} \tag{9}$$

where $\hat{K}_0 = (\hat{a}^\dagger\hat{a} + 1/2)/2$, $\hat{K}_+ = (\hat{a}^\dagger)^2/2$, $\hat{K}_- = \hat{a}^2/2$, and they satisfy the commutation relations $[\hat{K}_0, \hat{K}_\pm] = \pm\hat{K}_\pm$, $[\hat{K}_+, \hat{K}_-] = -2\hat{K}_0$. In the same way, Eq. (8) has the form

$$\begin{aligned}\hat{H}_{sp,\tilde{g}>1} = {} & \left(2\omega_r - \frac{\omega_r}{\tilde{g}^4}\right)\hat{K}_0 - \frac{\omega_r}{2\tilde{g}^4}(\hat{K}_+ + \hat{K}_-) \\ & - \frac{\omega_q(\tilde{g}^2 + \tilde{g}^{-2}) + 2\omega_r}{4}.\end{aligned} \tag{10}$$

By use of Bogoliubov-Valatin transformation, the above Hamiltonians can be diagonalized (see Appendix B). The diagonalized form of $\hat{H}_{np,\tilde{g}\leqslant 1}$ is $\omega_r\sqrt{1 - \tilde{g}^2}(\hat{b}^\dagger\hat{b} + 1/2) - (\omega_r + \omega_q)/2$ with the transformed bosonic modes $\{\hat{b}, \hat{b}^\dagger\}$. The diagonalized form of $\hat{H}_{sp,\tilde{g}>1}$ is $\omega_r\sqrt{1 - 1/\tilde{g}^4}(\tilde{b}^\dagger\tilde{b} + 1/2) - [2\omega_r + (\tilde{g}^2 + \tilde{g}^{-2})\omega_q]/4$ with the transformed bosonic modes $\{\tilde{b}^\dagger, \tilde{b}\}$. The system undergoes the QPT when $\tilde{g} \to \tilde{g}_c = 1$. The excitation spectra of $\hat{H}_{np,\tilde{g}\leqslant 1}$ and $\hat{H}_{sp,\tilde{g}>1}$ are $\omega_r\sqrt{1 - \tilde{g}^2}/2$ and $\omega_r\sqrt{1 - 1/\tilde{g}^4}/2$, respectively, and they both become zero at the critical point. In Fig. 1 the excitation energies of $\hat{H}_{np,\tilde{g}\leqslant 1}$ and $\hat{H}_{sp,\tilde{g}>1}$ are plotted.

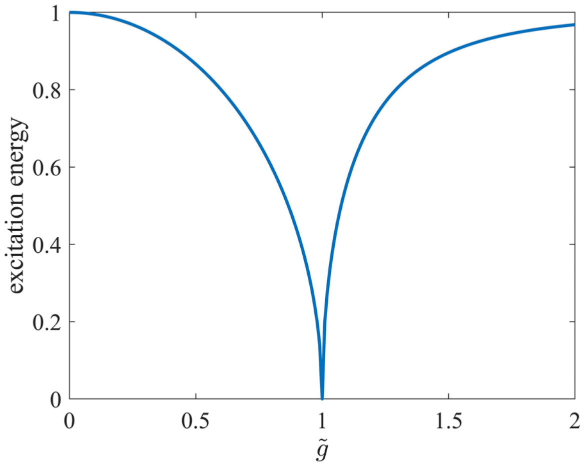

FIG. 1. Excitation energies of Hamiltonians $\hat{H}_{np,\tilde{g}\leqslant 1}$ and $\hat{H}_{sp,\tilde{g}>1}$ are $\omega_r\sqrt{1-\tilde{g}^2}/2$ and $\omega_r\sqrt{1-1/\tilde{g}^4}/2$, respectively. The QPT occurs at the critical point $\tilde{g}_c = 1$, where the excitation energies are both close to zero. Here $\omega_r = 1$ is set.

III. THE TIME SCALING OF THE QFI AROUND THE CRITICAL POINT

Quantum sensing aims at ultraprecise achievements of unknown parameters by exploiting unique quantum features, which can be assessed by the theory of quantum parameter estimation [41,42]. The estimating precision of a single unknown parameter is limited by the QCRB, which is determined by the QFI [42]. The QFI is dependent on the initial probe state, quantum dynamics, and evolution time. In this and next sections, we will investigate the time behavior of QFI of $\tilde{g}$ at the critical point and its dependence on the initial probe state.

For the parameter $\tilde{g}$ defined in Eq. (7), the upper bound of its estimation precision is given by the QCRB

$$\delta\tilde{g}^2 \geqslant \frac{1}{\nu I_{\tilde{g}}(T)}, \tag{11}$$

where ν is the number of trials and $I_{\tilde{g}}(T)$ is the QFI of $\tilde{g}$ with the total evolution time T. When the initial state is a pure state, $I_{\tilde{g}}(T)$ can be given by [4,41]

$$I_{\tilde{g}}(T) = 4\mathrm{Var}[h_{\tilde{g}}(T)]_{|\psi_0\rangle}, \tag{12}$$

where $\mathrm{Var}[\bullet]_{|\psi_0\rangle}$ represents the variance in the initial probe state $|\psi_0\rangle$. In Eq. (12), $h_{\tilde{g}}(T)$ is the generator of infinitesimal variations of $\tilde{g}$ [43],

$$\begin{aligned} h_{\tilde{g}}(T) &= i(\partial_{\tilde{g}} e^{-i\hat{H}(\tilde{g})T})e^{i\hat{H}(\tilde{g})T} \\ &= i\sum_{n=0}^{\infty}\frac{(-iT)^{n+1}}{(n+1)!}\hat{H}(\tilde{g})^{\times n}[\partial_{\tilde{g}}\hat{H}(\tilde{g})], \end{aligned} \tag{13}$$

where $\hat{A}^{\times n}(\bullet) := \overbrace{[\hat{A}, [\hat{A}, \cdots [\hat{A}}^{n \text{ times}}, \bullet]$ represents the nested commutators. In the above derivations, the derivative of an exponential operator $\partial_\ell e^{\hat{A}} = \int_0^1 ds\, e^{s\hat{A}}(\partial_\ell \hat{A})e^{(1-s)\hat{A}}$ and the well-known expansion $e^{\hat{A}}\hat{B}e^{-\hat{A}} = \hat{B} + [\hat{A}, \hat{B}] + (1/2!)[\hat{A}, [\hat{A}, \hat{B}]] + \cdots$ have been employed [44].

Inserting Eqs. (9) into (13), we obtain the generator for $\tilde{g} \leqslant 1$ (see Appendix C)

$$h_{\tilde{g}\leqslant 1}(T) = f_x\hat{K}_0 + f_y(\hat{K}_+ + \hat{K}_-) + if_z(\hat{K}_+ - \hat{K}_-), \tag{14}$$

where

$$\begin{aligned} f_x &= -2\tilde{g}T\omega_r + \frac{\tilde{g}^3}{2(1-\tilde{g}^2)^{3/2}}[\sin(2T\omega_r\sqrt{1-\tilde{g}^2}) - 2T\omega_r\sqrt{1-\tilde{g}^2}], \\ f_y &= -\tilde{g}T\omega_r + \frac{-2\tilde{g}+\tilde{g}^3}{4(1-\tilde{g}^2)^{3/2}}[\sin(2T\omega_r\sqrt{1-\tilde{g}^2}) - 2T\omega_r\sqrt{1-\tilde{g}^2}], \\ f_z &= \frac{\tilde{g}}{2(\tilde{g}^2-1)}[\cos(2T\omega_r\sqrt{1-\tilde{g}^2}) - 1]. \end{aligned} \tag{15}$$

Upon substituting Eqs. (10) into (13), we also have the generator for $\tilde{g} > 1$,

$$h_{\tilde{g}>1}(T) = \tilde{f}_x\hat{K}_0 + \tilde{f}_y(\hat{K}_+ + \hat{K}_-) + i\tilde{f}_z(\hat{K}_+ - \hat{K}_-) + \tilde{f}_h, \tag{16}$$

where

$$\begin{aligned} \tilde{f}_x &= \frac{4T\omega_r}{\tilde{g}^5} - \frac{1}{\tilde{g}^9(1-1/\tilde{g}^4)^{3/2}}[\sin(2T\omega_r\sqrt{1-1/\tilde{g}^4}) - 2T\omega_r\sqrt{1-1/\tilde{g}^4}], \\ \tilde{f}_y &= \frac{2T\omega_r}{\tilde{g}^5} + \frac{2\tilde{g}^4-1}{2\tilde{g}^9(1-1/\tilde{g}^4)^{3/2}}[\sin(2T\omega_r\sqrt{1-1/\tilde{g}^4}) - 2T\omega_r\sqrt{1-1/\tilde{g}^4}], \\ \tilde{f}_z &= \frac{-1}{\tilde{g}-\tilde{g}^5}[\cos(2T\omega_r\sqrt{1-1/\tilde{g}^4}) - 1], \\ \tilde{f}_h &= \frac{-T\omega_q(\tilde{g}^4-1)}{2\tilde{g}^3}. \end{aligned} \tag{17}$$

From Eqs. (14) and Eq. (12), one can obtain the QFI for $\tilde{g} \leqslant 1$

$$\begin{aligned} I_{\tilde{g}\leqslant 1}(T) = 4\big[&f_x^2\big(\langle \hat{K}_0^2\rangle_0 - \langle \hat{K}_0\rangle_0^2\big) + f_y^2\big(\langle(\hat{K}_+ + \hat{K}_-)^2\rangle_0 - \langle \hat{K}_+ + \hat{K}_-\rangle_0^2\big) - f_z^2\big(\langle(\hat{K}_+ - \hat{K}_-)^2\rangle_0 - \langle \hat{K}_+ - \hat{K}_-\rangle_0^2\big) \\ &+ f_x f_y(\langle \hat{K}_0(\hat{K}_+ + \hat{K}_-) + (\hat{K}_+ + \hat{K}_-)\hat{K}_0\rangle_0 - 2\langle \hat{K}_0\rangle_0\langle \hat{K}_+ + \hat{K}_-\rangle_0) \\ &+ i f_x f_z(\langle \hat{K}_0(\hat{K}_+ - \hat{K}_-) + (\hat{K}_+ - \hat{K}_-)\hat{K}_0\rangle_0 - 2\langle \hat{K}_0\rangle_0\langle \hat{K}_+ - \hat{K}_-\rangle_0) \\ &+ i f_y f_z(\langle(\hat{K}_+ + \hat{K}_-)(\hat{K}_+ - \hat{K}_-)\rangle_0 + \langle(\hat{K}_+ - \hat{K}_-)(\hat{K}_+ + \hat{K}_-)\rangle_0 - 2\langle \hat{K}_+ + \hat{K}_-\rangle_0\langle \hat{K}_+ - \hat{K}_-\rangle_0)\big], \end{aligned} \tag{18}$$

where $\langle \bullet \rangle_0$ denotes the expectation in the parameter-independent probe state $|\psi_0\rangle$. The QFI ($I_{\tilde{g}>1}(T)$) for $\tilde{g} > 1$ has the same form as Eq. (18) except that f_x, f_y, f_z are replaced by $\tilde{f}_x, \tilde{f}_y, \tilde{f}_z$, which are defined in Eq. (17).

Since all the expectations in Eq. (18) are independent of time, the time behavior of the QFI at the critical point is completely determined by the functions f_x, f_y, and f_z. Expanding those functions around the critical point ($\tilde{g}_c = 1$), $f_x \sim -\frac{2}{3}\omega_r^3 T^3$, $f_y \sim \frac{1}{3}\omega_r^3 T^3$ and $f_z \sim \omega_r^2 T^2$, we have

$$I_{\tilde{g}\leqslant 1}(T) \sim A\omega_r^6 T^6, \tag{19}$$

where A is a front factor dependent on the specific probe state. The time behavior of $I_{\tilde{g}>1}(T)$ for $\tilde{g} > 1$ is the same as Eq. (19), only with the different front factor. In addition, from Sec. II we can see that the parameters of an ion trap system, such as the coupling strength Ω_0, the frequency of spin transition ω_q, and the ion mass m, are all encoded in the parameter $\tilde{g}$. Thus, the QFIs of those parameters can be directly deduced from the QFI of $\tilde{g}$, i.e., $I_\xi(T) = (\partial_\xi \tilde{g})^2 I_{\tilde{g}}(T)$ for the parameter $\xi \in \{\Omega_0, \omega_q, m\}$. In general, one can directly obtain the QFIs of a parameter ξ from the QFI of $\tilde{g}$ if the condition $\partial_\xi \hat{H}(\tilde{g}) = \partial_{\tilde{g}}\hat{H}(\tilde{g})(\partial_\xi \tilde{g}) + C_0(\xi)$ is satisfied, where $C_0(\xi)$ is a function of ξ (see Appendix C).

From above, we see that the scaling T^6 of the QFI at the critical point with respect to the evolution time of the coding parameter dynamics is independent of the initial probe state and the estimating parameter. It is the critical behavior of the system under consideration and universal. Based on this time scaling, one may expect that the ultraprecision of parameter measurements could be achieved better than the Heisenberg limit T^2. In the following, however, we will show that the measurement precision here is not possible beyond the Heisenberg limit because of the restriction of the input energy during the measurement.

IV. THE ENERGY SCALING OF THE QFI AROUND THE CRITICAL POINT

As is well known, a physics measurement process must be involved with input-output energy. It may be meaningless when assessing the precision of measurement without considering the consuming energy in the implemented measurement. In this section we will use the average phonon number $\langle\psi_0|e^{i\hat{H}(\tilde{g})T}\hat{a}^\dagger\hat{a}e^{-i\hat{H}(\tilde{g})T}|\psi_0\rangle$ to measure the energy involved in the measurement. To this end, we will consider different probe initial states $|\psi_0\rangle$.

A. Coherent state

When the initial probe state is a coherent state $|\alpha\rangle$ with $\hat{a}|\alpha\rangle = \alpha|\alpha\rangle$ ($\alpha = \mathrm{Re}[\alpha] + i\mathrm{Im}[\alpha]$ is a complex number), from Eq. (18), the QFI can be obtained:

$$\begin{aligned} I_{\tilde{g}\leqslant 1}(T) = {}& f_x^2(\mathrm{Re}^2[\alpha] + \mathrm{Im}^2[\alpha]) \\ &+ \big(f_y^2 + f_z^2\big)(2 + 4\mathrm{Re}^2[\alpha] + 4\mathrm{Im}^2[\alpha]) \\ &+ 4f_x f_y\big(\mathrm{Re}^2[\alpha] - \mathrm{Im}^2[\alpha]\big) + 8f_x f_z \mathrm{Re}[\alpha]\mathrm{Im}[\alpha]. \end{aligned} \tag{20}$$

At the critical point, one has

$$I_{\tilde{g}\leqslant 1}(T) \sim \tfrac{2}{9}(1 + 8\mathrm{Im}^2[\alpha])\omega_r^6 T^6. \tag{21}$$

In Eq. (21), one may notice that only the imaginary part of the state is in the QFI at the critical point. It means that a strong local oscillator is required as a phase reference. At the time T, the average phonon number around the critical point is $\langle N\rangle \approx (1 + 4\mathrm{Im}[\alpha]^2)\omega_r^2 T^2$ (see Appendix D). Thus, $I_{\tilde{g}\leqslant 1}(T) \sim \langle \hat{N}\rangle^2 T^2$. It is just the Heisenberg limit (HL). For the case $\tilde{g} > 1$, we have the same result.

B. Fock state

When the initial probe state is a Fock state $|n\rangle$, from Eq. (18), we have

$$I_{\tilde{g}\leqslant 1}(T) = 2\big(f_y^2 + f_z^2\big)(n^2 + n + 1). \tag{22}$$

Around the critical point, the QFI can be approximated to

$$I_{\tilde{g}\leqslant 1}(T) \sim \frac{2}{9}(n^2 + n + 1)\omega_r^6 T^6. \tag{23}$$

Since the average phonon number around the critical point is $\langle N\rangle \approx (1 + 2n)\omega_r^2 T^2/4$, the QFI can be written as $I_{\tilde{g}\leqslant 1}(T) \sim \langle \hat{N}\rangle^2 T^2$ at the critical point, just being the HL. For the case $\tilde{g} > 1$, we have the same result.

C. Superposition state

Here we consider the superposition state $(|0\rangle + i|n\rangle)/\sqrt{2}$ as the initial probe state. From Eq. (18), we have the QFI

$$I_{\tilde{g}\leqslant 1}(T) = \begin{cases} f_x^2 + 8f_y^2 + 6f_z^2 & n = 2 \\ 4f_x^2 + 22\big(f_x^2 + f_z^2\big) + 4\sqrt{6}f_y f_z & n = 4 \\ \frac{n^2}{4}f_x^2 + (n^2 + n + 2)\big(f_x^2 + f_z^2\big) & n \neq \{2, 4\} \end{cases}. \tag{24}$$

Equation (24) implies that the QFI can be improved with increasing n, as shown in Fig. 2(a). At the critical point,

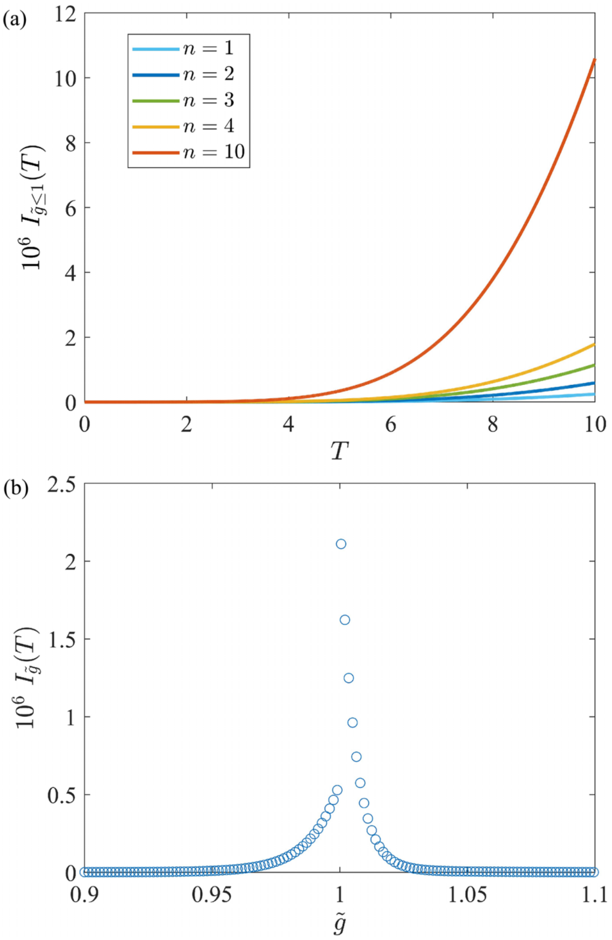

FIG. 2. QFI of $\tilde{g}$ with the initial state $(|0\rangle + i|n\rangle)/\sqrt{2}$. (a) The QFI is plotted as a function of the total evolution time T for $n = \{1, 3, 5, 12\}$, respectively. Here $\omega_r = 1$, $\tilde{g} = 0.99$ are set; (b) the QFI vs the parameter $\tilde{g}$ with the initial state $(|0\rangle + i|1\rangle)/\sqrt{2}$. Here $\omega_r = 1$, $T = 10$, $n = 1$ are set.

Eq. (24) is approximated to

$$I_{\tilde{g}\leqslant 1}(T) \sim \begin{cases} \frac{4}{3}\omega_r^6 T^6 & n = 2 \\ \frac{104}{9}\omega_r^6 T^6 & n = 4 \\ \frac{1}{9}(5n^2 + 4n + 8)\omega_r^6 T^6 & n \neq \{2, 4\} \end{cases}. \tag{25}$$

In this case, the average phonon number around the critical point is $\langle N\rangle \approx (1 + n)\omega_r^2 T^2/4$. As a result, we have $I_{\tilde{g}\leqslant 1}(T) \sim \langle \hat{N}\rangle^2 T^2$. Therefore, the HL can also be achieved. For the case $\tilde{g} > 1$, we have the same result.

In Fig. 2(b) the QFI is plotted as a function of $\tilde{g}$. The peak feature of the QFI around the critical point implies that the ultraprecision of estimation of $\tilde{g}$ may be attained around the critical point.

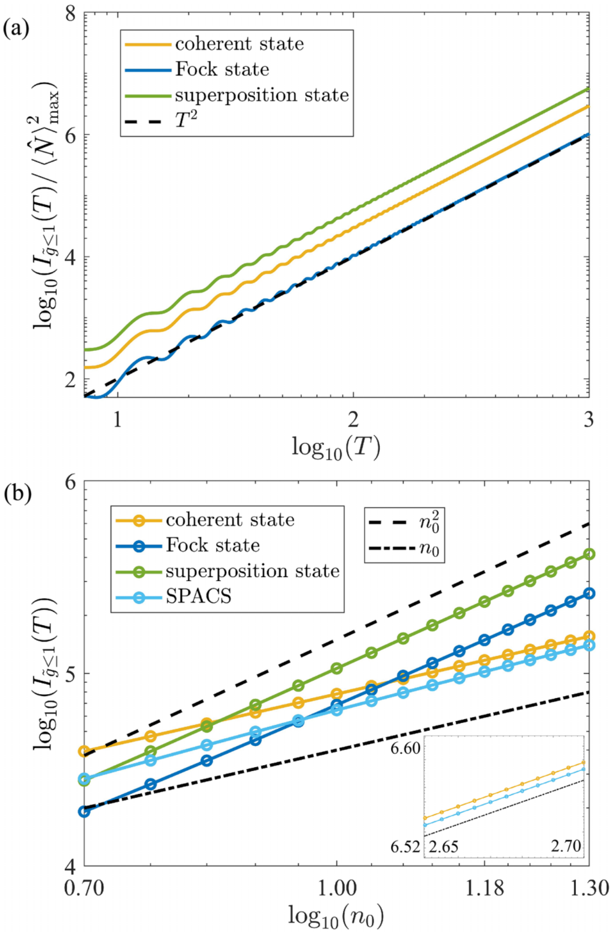

FIG. 3. (a) The QFI $I_{\tilde{g}\leqslant 1}(T)$ scaled by $\langle \hat{N}\rangle^2_{\max}$ is as a function of the total evolution time T for the different initial probe states. The black dashed line stands for the Heisenberg scaling T^2. The yellow, blue, and green lines are for the coherent state $|\alpha\rangle$, Fock state $|n\rangle$, and superposition state$(|0\rangle + i|n\rangle)/\sqrt{2}$, respectively. Here $\tilde{g} = 0.9$, $\alpha = \sqrt{10}i$, $n = 10$ are set. (b) The QFI $I_{\tilde{g}\leqslant 1}(T)$ vs the initial phonon number n_0 for the different probe states. The black dashed lines stand for the Heisenberg scaling n_0^2 and the SQL scaling n_0. The yellow, blue, green, and cyan lines are for the coherent state $|\alpha\rangle$, Fock state $|n\rangle$, superposition state $(|0\rangle + i|n\rangle)/\sqrt{2}$, and SPACS $|\alpha, 1\rangle$, respectively. Here $\tilde{g} = 0.9$, $T = 10$ are set. The inset shows the scaling of the QFI for the coherent state and SPACS when n_0 is large.

The average phonon numbers during the evolution may be different for different initial probe states. In order to compare the QFIs with the equal average phonon number, we rescale the QFI by $\langle \hat{N}\rangle^2_{\max}$ which is the maximum of the average phonon number during the evolution for each of the initial probe states with respect to the evolution time T (see Appendix D). In Fig. 3(a) the rescaled QFI is plotted as a function of the total evolution time T. It is clearly observed that all the states such as the coherent state, Fock state, and superposition state can reach the same Heisenberg scaling T^2.

The different probe states have the different initial average phonon numbers. In the following discussion, we set that all the probe states have the same initial phonon number $\langle\psi_0|\hat{N}|\psi_0\rangle_0 = n_0$. In Fig. 3(b) the QFI is plotted as a function of n_0.

One can see that the Fock and superposition states can reach the Heisenberg scaling $\langle \hat{N}\rangle^2$, but the coherent state remains the standard quantum limit (SQL) scaling. It reminds us that the Heisenberg scaling $\langle \hat{N}\rangle^2$ may result from the nonclassical properties of the probe state. In order to check this point, we consider the single-photon (phonon) -added coherent state (SPACS): $|\alpha, 1\rangle = \hat{a}^\dagger|\alpha\rangle/\sqrt{1+|\alpha|^2}$, which is an intermediate state between the Fock state and the coherent state, and exhibits the nonclassical behavior when the coherent amplitude is small [45]. As noted, when n_0 is small, the SPACS surpasses the SQL. As n_0 increases, the scaling of the SPACS returns to SQL. This change is attributed to the fact that the SPACS gradually becomes the coherent state and loses the nonclassical behavior as α increases [45]. The result indicates that nonclassical propoerties of the probe states may also be a quantum resource for quantum sensing to break the SQL.

V. EFFECT OF DIFFERENT MEASUREMENT SCHEMES ON THE ESTIMATION PRECISION

In order to extract the true value of the parameter $\tilde{g}$ from the coded state $|\psi(T, \tilde{g})\rangle = e^{-i\hat{H}(\tilde{g})T}|\psi_0\rangle$, one needs to choose an appropriate operator $\hat{O}$ and perform the corresponding measurement on the coded state. According to the error propagation formula, the inverted variance for the estimation of $\tilde{g}$ is determined by [9,46]

$$\mathcal{F}_{\tilde{g}}(T) = \left(\frac{\partial_{\tilde{g}}\langle\hat{O}\rangle_T}{\langle\Delta\hat{O}\rangle_T}\right)^2. \tag{26}$$

Then we obtain the variance $\delta\tilde{g}^2 = 1/(\nu\mathcal{F}_{\tilde{g}}(T))$, where ν is the number of measurements.

On the other hand, the estimation variance is lower bounded by the quantum Fisher information as shown in Eq. (11):

$$\delta\tilde{g}^2 \geqslant \frac{1}{\nu I_{\tilde{g}}(T)}. \tag{27}$$

The left side of Eq. (27) does depend on the chosen measurement scheme. One may make the equality hold by optimizing the measurement scheme and attain the highest precision. In the following, we will consider two measurement schemes: the homodyne detection and the average phonon number detection, respectively.

A. Homodyne detection

Let us suppose that the initial probe state is $(|0\rangle + i|1\rangle)/\sqrt{2} \otimes |\downarrow\rangle$, where $|\downarrow\rangle$ and $(|0\rangle + i|1\rangle)/\sqrt{2}$ are the electronic state of the ion and the phonon state of the center-mass motion, respectively. In order to extract the value of $\tilde{g}$, we choose the quadrature operator $\hat{X}$ or $\hat{P}$ as the measurement operator, which are defined as

$$\hat{X} = (\hat{a} + \hat{a}^\dagger)/\sqrt{2}, \quad \hat{P} = i(\hat{a}^\dagger - \hat{a})/\sqrt{2}. \tag{28}$$

In terms of the quadrature operators, the Hamiltonian (6) can be rewritten as

$$\hat{H}_{np,\tilde{g}\leqslant 1} = \frac{\omega_r}{2}[\hat{P}^2 + (1-\tilde{g}^2)\hat{X}^2]. \tag{29}$$

In the Heisenberg picture, we have the equations of motion for the quadrature operators with Hamiltonian (29):

$$\frac{d\hat{X}}{dT} = -i[\hat{X}, \hat{H}_{np,\tilde{g}\leqslant 1}] = \omega_r\hat{P}, \tag{30}$$

$$\frac{d\hat{P}}{dT} = -i[\hat{P}, \hat{H}_{np,\tilde{g}\leqslant 1}] = -(1-\tilde{g}^2)\omega_r\hat{X}. \tag{31}$$

Solving Eq. (29) with the initial conditions $\langle\hat{X}\rangle_0 = 0$, $\langle\hat{P}\rangle_0 = 1/\sqrt{2}$, we obtain the expectation value of $\hat{X}$ at the evolution time T,

$$\langle\hat{X}\rangle_T = \frac{\sin(\sqrt{1-\tilde{g}^2}\omega_r T)}{\sqrt{2(1-\tilde{g}^2)}}, \tag{32}$$

then

$$\partial_{\tilde{g}}\langle\hat{X}\rangle_T = 2\tilde{g}\bigg[-1+\cos(2\sqrt{1-\tilde{g}^2}T\omega_r) + \frac{\tilde{g}^2 T\omega_r\sin(2\sqrt{1-\tilde{g}^2}T\omega_r)}{\sqrt{1-\tilde{g}^2}}\bigg]. \tag{33}$$

For the variance of $\hat{X}$, we solve the following equations:

$$\frac{d\hat{X}^2}{dT} = \omega_r(\hat{X}\hat{P} + \hat{P}\hat{X}), \tag{34}$$

$$\frac{d\hat{P}^2}{dT} = -(1-\tilde{g}^2)\omega_r(\hat{X}\hat{P} + \hat{P}\hat{X}), \tag{35}$$

$$\frac{d(\hat{X}\hat{P} + \hat{P}\hat{X})}{dT} = 2\omega_r[\hat{P}^2 - (1-\tilde{g}^2)\hat{X}^2], \tag{36}$$

and attain

$$\langle(\Delta\hat{X})^2\rangle = \frac{(2\tilde{g}^2-1)\cos(2\sqrt{1-\tilde{g}^2}\omega_r T) + 2\tilde{g}^2 - 3}{4(\tilde{g}^2-1)}. \tag{37}$$

Inserting Eqs. (33) and (37) into (26), we obtain the inverted variance of the estimating value of $\tilde{g}$, which is plotted as a function of the rescaled time t in Fig. 4(a). The ratio of $I_{\tilde{g}\leqslant 1}(t)$ to $\mathcal{F}_{\tilde{g}}(t)$ is plotted in Fig. 4(b). We notice that in Fig. 4(a) and Fig. 4(b) the peaks appear at the moment $T = n\pi/(\sqrt{1-\tilde{g}^2}\omega_r)$ $(n = 1, 2, \ldots)$. It means that the highest precision with the homodyne detection scheme is achieved at those points. As shown in Fig. 4(b), the ratio is less than one. Thus, employing the homodyne detection scheme, one cannot attain the highest possible precision which is allowed by quantum principle.

In Fig. 4(c) the ratio of $I_{\tilde{g}\leqslant 1}(t)$ to $\mathcal{F}_{\tilde{g}}(t)$ is plotted as a function of $\tilde{g}$ from the normal phase to the superradiant phase. It is observed that the inverted variance approximately reaches the same scaling as the QFI of $\tilde{g}$ (25) [i.e., $\mathcal{F}_{\tilde{g}}(t)/I_{\tilde{g}}(t) \simeq 0.4$] near the critical point $\tilde{g} = 1$. The homodyne detection is feasible in experiment and has been performed in many platforms, including ion traps [34].

B. Average phonon number detection

Now we consider the average phonon number detection scheme [47]. In this case the initial probe state is taken as $|1\rangle \otimes |\downarrow\rangle$ and the phonon number operator is chosen as the measurement operator, which is defined as

$$\hat{N} = \hat{a}^\dagger\hat{a} = 2\hat{K}_0 - \tfrac{1}{2}. \tag{38}$$

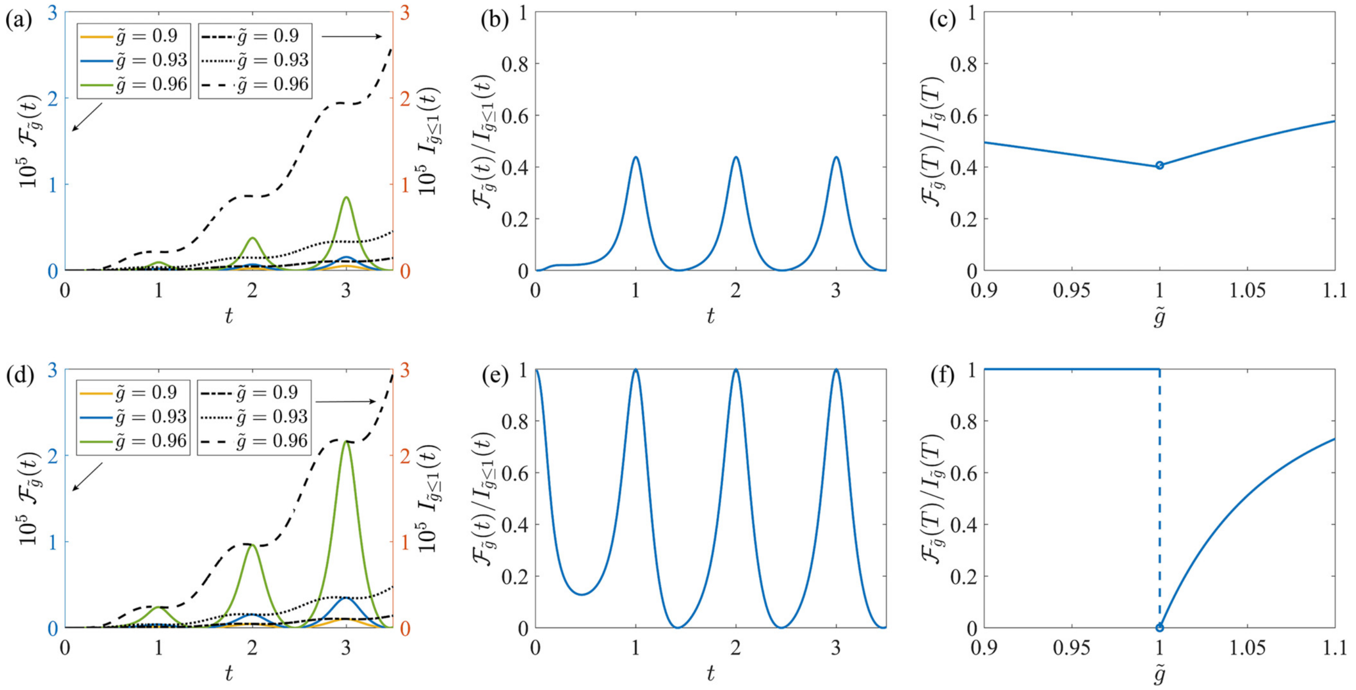

FIG. 4. (a, b) The inverted variance $\mathcal{F}_{\tilde{g}}(t)$ vs the QFI $I_{\tilde{g}\leqslant 1}(t)$ with the quadrature $\hat{X}$ detection scheme is displayed as a function of the evolution time t that is scaled by $\sqrt{1-\tilde{g}^2}\omega_r T/\pi$. The initial probe state is $(|0\rangle + i|1\rangle)/\sqrt{2} \otimes |\downarrow\rangle$. (d,e) The inverted variance $\mathcal{F}_{\tilde{g}}(t)$ vs the QFI $I_{\tilde{g}\leqslant 1}(t)$ with the average phonon number detection scheme is displayed as a function of the evolution time t that is scaled by $\sqrt{1-\tilde{g}^2}\omega_r T/\pi$. The initial probe state is $|1\rangle \otimes |\downarrow\rangle$. In (a) and (d), the solid lines are for $\mathcal{F}_{\tilde{g}}(t)$ in the unit on the left side of the y axis, and the dashed lines are for the QFI $I_{\tilde{g}\leqslant 1}(t)$ in the unit on the right side of the y axis. In (b) and (e), the ratio of $\mathcal{F}_{\tilde{g}}(t)$ to $I_{\tilde{g}\leqslant 1}(t)$ as a function of the evolution time t with $\tilde{g} = 0.96$, and the peak value in (b) is about 0.43. In (c) and (f), the ratio of $\mathcal{F}_{\tilde{g}}(T)$ to $I_{\tilde{g}}(T)$ as a function of the parameter $\tilde{g}$ from the normal phase to the superradiant phase with the evolution time $t = 1$ standing for a period. The value of the ratio is about 0.4 when $\tilde{g}$ approaches $\tilde{g}_c = 1$ in (c). $T = \pi/(\sqrt{1-\tilde{g}^2}\omega_r)$ in the normal phase and $T = \pi/(\sqrt{1-1/\tilde{g}^4}\omega_r)$ in the superradiant phase are set.

In the Heisenberg picture, we solve the equations of motion with the Hamiltonian (9):

$$\frac{d\hat{K}_0}{dT} = -i[\hat{K}_0, \hat{H}_{np,\tilde{g}\leqslant 1}] = \frac{1}{2} i\omega_r \tilde{g}^2 (\hat{K}_+ - \hat{K}_-), \tag{39}$$

$$\frac{d(\hat{K}_+ - \hat{K}_-)}{dT} = -i[\hat{K}_+ - \hat{K}_-, \hat{H}_{np,\tilde{g}\leqslant 1}] = i\omega_r((2-\tilde{g}^2)(\hat{K}_+ + \hat{K}_-) - 2\tilde{g}^2\hat{K}_0), \tag{40}$$

$$\frac{d(\hat{K}_+ + \hat{K}_-)}{dT} = -i[\hat{K}_+ + \hat{K}_-, \hat{H}_{np,\tilde{g}\leqslant 1}] = i\omega_r(2-\tilde{g}^2)(\hat{K}_+ - \hat{K}_-), \tag{41}$$

with the initial conditions $\langle\hat{K}_0\rangle_0 = \frac{3}{4}$, $\langle\hat{K}_+ - \hat{K}_-\rangle_0 = 0$, $\langle\hat{K}_+ + \hat{K}_-\rangle_0 = 0$. The average phonon number at the time T is given by

$$\langle\hat{N}\rangle_T = 1 + 3\tilde{g}^4(8 - 8\tilde{g}^2)^{-1}[1 - \cos(\sqrt{4(1-\tilde{g}^2)}\omega_r T)]. \tag{42}$$

Similarly, we also obtain

$$\partial_{\tilde{g}}\langle\hat{N}\rangle_T = 3\tilde{g}^3 \sin(\sqrt{1-\tilde{g}^2}T\omega_r)\left[-\frac{\tilde{g}^2 T\omega_r \cos(\sqrt{1-\tilde{g}^2}T\omega_r)}{(1-\tilde{g}^2)^{3/2}} - \frac{(\tilde{g}^2-2)\sin(\sqrt{1-\tilde{g}}T\omega_r)}{(\tilde{g}^2-1)^2}\right], \tag{43}$$

$$\langle(\Delta\hat{N})^2\rangle_T = \frac{3\tilde{g}^4 \sin^2(\sqrt{1-\tilde{g}^2}\omega_r T)}{16(\tilde{g}^2-1)^2}[-\tilde{g}^4 + 8\tilde{g}^2 - 8 + \tilde{g}^4\cos(2\sqrt{1-\tilde{g}^2}\omega_r T)]. \tag{44}$$

Inserting Eqs. (43) and (44) into (26), one can obtain the inverted variance of the estimated value of $\tilde{g}$, which is plotted in Fig. 4(d). For comparison, the QFI is also plotted in Fig. 4(d). It is observed that the measurement precision attained by the average phonon number detection scheme can reach the QCRB at the time points $T = n\pi/(\sqrt{1-\tilde{g}^2}\omega_r)$ ($n = 1, 2, \ldots$). The ratio of $\mathcal{F}_{\tilde{g}}(t)$ to $I_{\tilde{g}\leqslant 1}(t)$ is plotted in Fig. 4(e) and Fig. 4(f). We can see that the highest estimation precision allowed by quantum mechanics is obtained only in the normal

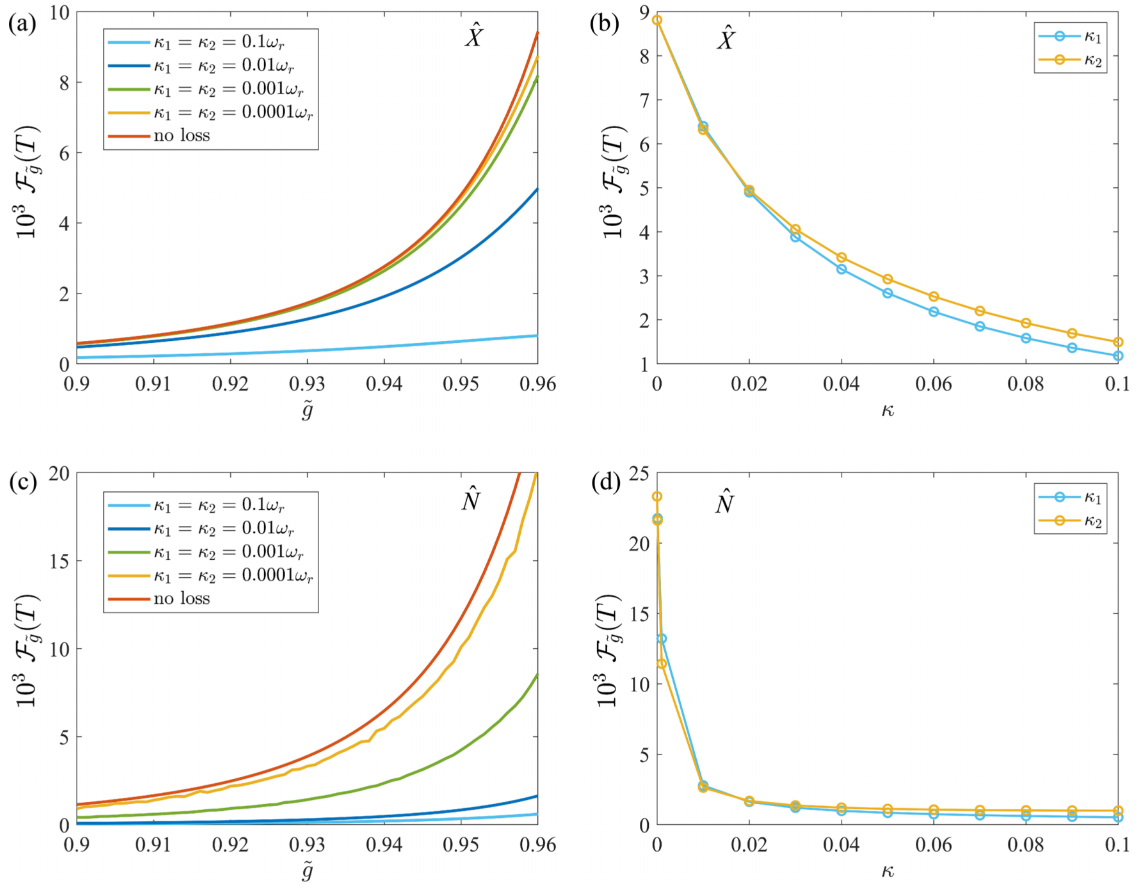

FIG. 5. The inverted variance $\mathcal{F}_{\tilde{g}}(T)$ of the quadrature $\hat{X}$ and the phonon number $\hat{N}$ in the dissipative case. $T = \pi/(\sqrt{1-\tilde{g}^2}\omega_r)$ is set. (a) The inverted variance $\mathcal{F}_{\tilde{g}}(T)$ of $\hat{X}$ for various values of κ_1 and κ_2. (b) The inverted variance $\mathcal{F}_{\tilde{g}}(T)$ of $\hat{X}$ as a function of the decay rate κ_1 (heating rate κ_2) and $\kappa_2 = 0$ ($\kappa_1 = 0$), $\tilde{g} = 0.96$ are set. (c) The inverted variance $\mathcal{F}_{\tilde{g}}(T)$ of $\hat{N}$ for various values of the decay and heating rates $\kappa_1,\ \kappa_2$. (d) The inverted variance $\mathcal{F}_{\tilde{g}}(T)$ of $\hat{N}$ as a function of the decay rate κ_1 (heating rate κ_2) and $\kappa_2 = 0(\kappa_1 = 0),\ \tilde{g} = 0.96$ are set.

phase. The average phonon detection is also experimentally feasible for ion trap systems [35].

C. Dissipative case

In practical ion trap systems, the influence of noise is unavoidable and must be taken into account. Here we consider the interaction between the phonon and the environment. The time evolution of the density matrix of the system with the Hamiltonian (4) is governed by the master equation

$$\frac{\partial \rho}{\partial t} = -i[\hat{H}_{\mathrm{QRM}}, \rho] + \kappa_1 \mathcal{D}[\hat{a}]\rho + \kappa_2 \mathcal{D}[\hat{a}^\dagger]\rho, \tag{45}$$

where κ_1, κ_2 are the decay and heating rates of phonon, respectively, and the Lindblad terms read $\mathcal{D}[\hat{A}]\rho = 2\hat{A}\rho\hat{A}^\dagger - \{\hat{A}^\dagger\hat{A}, \rho\}$.

Applying the SW transformation $U_{np} = \exp[-(g/\omega_q)(\hat{a} + \hat{a}^\dagger)(\hat{\sigma}_+ - \hat{\sigma}_-)]$ to Eq.(45) (see Appendix A), one can project it in the spin-down subspace, and obtain the effective master equation [48]

$$\frac{\partial \rho_a}{\partial t} = -i[\hat{H}_{np,\tilde{g}\leqslant 1}, \rho_a] + \kappa_1 \mathcal{D}[\hat{a}]\rho_a + \kappa_2 \mathcal{D}[\hat{a}^\dagger]\rho_a, \tag{46}$$

with $\rho_a \equiv \langle\downarrow| U_{np}^\dagger \rho U_{np} |\downarrow\rangle$.

Solving Eq. (46) numerically, we obtain the density matrix of the system and then work out the average values of the detection operators $\hat{X}$ and $\hat{N}$, and their variances. In Fig. 5(a) the inverted variance with the quadrature $\hat{X}$ is plotted for various values of the decay rates. It is noted that the enhanced sensing can be maintained under the finite noise level although the noise obviously affects the estimation precision. In Fig. 5(c) the inverted variance with the measurement operator $\hat{N}$ is plotted for various values of the decay rates. In Figs. 5(b) and 5(d) the effects of κ_1 and κ_2 on the estimation precision are shown respectively. One may notice that the average phonon detection is more sensitive to the noise.

VI. TWO-MODE NON-HERMITIAN SU(1,1) MODEL

In this section we extend the previous investigation to a two-mode SU(1,1) Hamiltonian and show that across the exceptional point (EP) the QFI exhibits the same behavior as in the QRM.

The two-mode bosonic model is described by the Hamiltonian

$$\mathcal{H} = \delta(\hat{a}_1^\dagger\hat{a}_1 + \hat{a}_2^\dagger\hat{a}_2) + \alpha_0(\hat{a}_1^\dagger\hat{a}_2^\dagger + \hat{a}_1\hat{a}_2), \tag{47}$$

where $\hat{a}_j$ and $\hat{a}_j^\dagger$ are the bosonic annihilation and creation operators for the jth mode, δ is frequency of the two modes, and α_0 is the coupling strength between the modes. In the Heisenberg picture, we have

$$i\partial_t(\hat{a}_1, \hat{a}_2^\dagger)^T = H_{\mathrm{APT}}(\hat{a}_1, \hat{a}_2^\dagger)^T, \tag{48}$$

with the non-Hermitian Hamiltonian matrix

$$H_{\mathrm{APT}} = \delta\hat{\sigma}_z - i\alpha_0\hat{\sigma}_y = \begin{pmatrix} \delta & \alpha_0 \\ -\alpha_0 & -\delta \end{pmatrix}. \tag{49}$$

Note that H_{APT} is non-Hermitian and satisfies the anticommutation relation $\{H_{\mathrm{APT}}, \mathcal{PT}\} = 0$, where the parity operator $\mathcal{P} = \hat{\sigma}_x$ and the time-reversal operator $\mathcal{T} = \mathcal{K}$ the complex conjugate. Thus, H_{APT} has the anti-parity-time ($\mathcal{APT}$) symmetry.

In the $\mathcal{APT}$-symmetric region with $|\delta| < |\alpha_0|$, the eigenvalues of H_{APT} are $\lambda_\pm = \pm i\lambda_0$ with $\lambda_0 = \sqrt{|\alpha_0^2 - \delta^2|}$. While in the $\mathcal{APT}$-broken region with $|\delta| > |\alpha_0|$, the eigenvalues of H_{APT} are $\lambda_\pm = \pm\lambda_0$. The spontaneous symmetry breaking occurs at the EP $|\alpha_0| = |\delta|$ [12].

We find that the Hamiltonian (47) also has the SU(1,1) dynamic symmetry, which can be rewritten as

$$\mathcal{H} = 2\delta\tilde{K}_0 + \alpha_0(\tilde{K}_+ + \tilde{K}_-) - \delta, \tag{50}$$

where $\tilde{K}_0 = (\hat{a}_1^\dagger\hat{a}_1 + \hat{a}_2^\dagger\hat{a}_2 + 1)/2$, $\tilde{K}_+ = \hat{a}_1^\dagger\hat{a}_2^\dagger$, $\tilde{K}_- = \hat{a}_1\hat{a}_2$, satisfying the commutation relations $[\tilde{K}_0, \tilde{K}_\pm] = \pm\tilde{K}_\pm$, $[\tilde{K}_+, \tilde{K}_-] = -2\tilde{K}_0$.

As done in the previous sections, we introduce the QFI for the estimation of the parameter α_0,

$$I_{\alpha_0}(T) = 4\mathrm{Var}\big[h_{\alpha_0}(T)\big]_{|\psi_0\rangle}, \tag{51}$$

where $h_{\alpha_0}(T)$ is the generator of infinitesimal variations of α_0 (see Appendix C),

$$h_{\alpha_0}(T) = f_1\tilde{K}_0 + f_2(\tilde{K}_+ + \tilde{K}_-) + if_3(\tilde{K}_+ - \tilde{K}_-), \tag{52}$$

with

$$\begin{aligned} f_1 &= \frac{\delta\alpha_0}{\left(\delta^2 - \alpha_0^2\right)^{3/2}}\Big[\sin\Big(2T\sqrt{\delta^2 - \alpha_0^2}\Big) - 2T\sqrt{\delta^2 - \alpha_0^2}\Big], \\ f_2 &= T + \frac{\delta\alpha_0}{\left(\delta^2 - \alpha_0^2\right)^{3/2}}\Big[\sin\Big(2T\sqrt{\delta^2 - \alpha_0^2}\Big) - 2T\sqrt{\delta^2 - \alpha_0^2}\Big], \\ f_3 &= \frac{\delta\alpha_0}{2\left(\delta^2 - \alpha_0^2\right)}\Big[\cos\Big(2T\sqrt{\delta^2 - \alpha_0^2}\Big) - 1\Big]. \end{aligned} \tag{53}$$

By substituting Eqs. (52) into Eq. (51), we find the QFI for the parameter α_0

$$\begin{aligned} I_{\alpha_0}(T) = 4\big[&f_1^2\big(\langle\tilde{K}_0^2\rangle_0 - \langle\tilde{K}_0\rangle_0^2\big) + f_2^2\big(\langle(\tilde{K}_+ + \tilde{K}_-)^2\rangle_0 - \langle\tilde{K}_+ + \tilde{K}_-\rangle_0^2\big) - f_3^2\big(\langle(\tilde{K}_+ - \tilde{K}_-)^2\rangle_0 - \langle\tilde{K}_+ - \tilde{K}_-\rangle_0^2\big) \\ &+ f_1f_2(\langle\tilde{K}_0(\tilde{K}_+ + \tilde{K}_-) + (\tilde{K}_+ + \tilde{K}_-)\tilde{K}_0\rangle_0 - 2\langle\tilde{K}_0\rangle_0\langle\tilde{K}_+ + \tilde{K}_-\rangle_0) \\ &+ if_1f_3(\langle\tilde{K}_0(\tilde{K}_+ - \tilde{K}_-) + (\tilde{K}_+ - \tilde{K}_-)\tilde{K}_0\rangle_0 - 2\langle\tilde{K}_0\rangle_0\langle\tilde{K}_+ - \tilde{K}_-\rangle_0) \\ &+ if_2f_3(\langle(\tilde{K}_+ + \tilde{K}_-)(\tilde{K}_+ - \tilde{K}_-)\rangle_0 + \langle(\tilde{K}_+ - \tilde{K}_-)(\tilde{K}_+ + \tilde{K}_-)\rangle_0 - 2\langle\tilde{K}_+ + \tilde{K}_-\rangle_0\langle\tilde{K}_+ - \tilde{K}_-\rangle_0)\big], \end{aligned} \tag{54}$$

where $\langle\bullet\rangle_0$ represents the expectation in the initial probe state $|\psi_0\rangle$. Expanding the functions (53) at the EP $\alpha_0 = \delta$, one can find that the QFI follows the same scaling law of AT^6 at the EP as Eq. (19). Here A is a front factor which is determined by the specific probe state.

VII. SUMMARY

The quantum Rabi model describes the interaction between the two inner states and quantum center-mass motion of a trapped ion. When the transition frequency between the two inner states is much larger than that of the external motion, the inner motion of the ion always remains in the inner lower state, and the Hamiltonian of the external motion can be written as a linear function of operators of the SU(1,1) algebra. This Hamiltonian exhibits a quantum phase transition as the coupling strength approaches the critical value. We investigate the critical properties of the QFI for the estimation of parameter at the critical point of the SU(1,1) dynamic system. We show that the QFI goes divergently in the sixth power law (T^6) of the parameter coding time around the critical point. A physical measurement must be involved with energy consumption. It is the best way that the consumption energy is as little as possible while attaining the possible highest measurement precision. In the present situation, it represents the phonon number of excitation during the parameter coding process. After taking into the consuming energy, we find that the variation of the QFI around the critical point is scaled by the Heisenberg limit T^2. It is noticed that for nonclassical initial probe states such as phonon number states, its linear superposition and the the single-photon(phonon)-added coherent state, the variation of the QFI surpasses the SQL n_0 as a function of the initial mean phonon number n_0. It implies that the nonclassical properties such as the negativity of Wigner function is also a resource for quantum sensing besides quantum coherent and entanglement, as proved in [49,50]. In order to attain the possible highest precision, the measurement scheme must be optimized. In this study, we compare the homodyne detection and the average phonon number detection schemes. We find that the quantum Cramér-Rao bound can be reached by use of the average phonon number detection scheme. However, it is more sensitive to the decay and heating of phonons than the homodyne detection scheme. In addition, we extend the study to a two-mode non-Hermitian system and show that the QFI exhibits the same anomalous feature at the exceptional point, revealing that the QFI universally diverges as T^6 at the critical point of the SU(1,1) dynamic systems. We believe that the critical properties of the QFI can be useful for quantum sensing and quantum parameter estimation.

ACKNOWLEDGMENTS

This research is supported by the National Natural Science Foundation of China (NSFC) (Grants No. 12074307, No. 12204371, No. 11804271, and No. 91736104), Shaanxi Fundamental Science Research Project for Mathematics and Physics (Grants No. 22JSQ035, No. 22JSZ004, and No. 23JSQ012), China Postdoctoral Science Foundation via Project No. 2020M673366, and Shaanxi Natural Science Basic Research Program (Grant No. 2021JQ-008).

APPENDIX A: THE SW TRANSFORMATION TO THE ORIGINAL HAMILTONIAN

In this Appendix, we perform Schrieffer-Wolff (SW) transformation to the Hamiltonian (4) [20]. For this purpose, we consider a unitary transformation $U = e^S$ to the original Hamiltonian (4). The transformed Hamiltonian can be written as

$$\hat{H}' = e^{-S}\hat{H}_{\mathrm{QRM}}e^{S} = \sum_{k=0}^{\infty}\frac{1}{k!}[\hat{H}_{\mathrm{QRM}}, S]^{(k)}, \tag{A1}$$

where $[\hat{H}_{\mathrm{QRM}}, S]^{(k)} \equiv [[\hat{H}_{\mathrm{QRM}}, S]^{(k-1)}, S]$, $[\hat{H}_{\mathrm{QRM}}, S]^{(0)} \equiv H$. For simplification, we need the nondiagonal elements of $\hat{H}'$ to be zero, which leads to

$$S = \frac{g}{\omega_q}(\hat{a}^\dagger + \hat{a})(\hat{\sigma}_+ - \hat{\sigma}_-) + O\left(\frac{\omega_r}{\omega_q^2}\right). \tag{A2}$$

Considering the limit $\omega_q/\omega_r \to \infty$, higher-order terms can be neglected. Then the transformed Hamiltonian becomes

$$\hat{H}' = \omega_r\hat{a}^\dagger\hat{a} + \frac{\omega_q}{2}\hat{\sigma}_z + \frac{\omega_r\tilde{g}^2}{4}(\hat{a}^\dagger + \hat{a})^2\hat{\sigma}_z, \tag{A3}$$

with $\tilde{g} = 2g/\sqrt{\omega_r\omega_q}$, and it can be projected to the spin subspace,

$$\hat{H}_{np,\tilde{g}\leqslant 1} = \omega_r\hat{a}^\dagger\hat{a} - \frac{\omega_q}{2} - \frac{\omega_r\tilde{g}^2}{4}(\hat{a}^\dagger + \hat{a})^2. \tag{A4}$$

For $\tilde{g} > 1$, the eigenvalue of the above Hamiltonian will be non-Hermitian. Therefore, we apply a unitary transformation $D(\alpha) = e^{\alpha(\hat{a}^\dagger - \hat{a})}$ to Eq. (4),

$$\begin{aligned}\tilde{H}_{\mathrm{QRM}} &= D^\dagger(\alpha)\hat{H}_{\mathrm{QRM}}D(\alpha)\\ &= \omega_r(\hat{a}^\dagger + \alpha)(\hat{a} + \alpha) + \frac{\omega_q}{2}\hat{\sigma}_z - \lambda(\hat{a} + \hat{a}^\dagger + 2\alpha)\hat{\sigma}_x.\end{aligned} \tag{A5}$$

After a similar process as before, it can be projected to the transformed spin-down subspace,

$$\hat{H}_{sp,\tilde{g}>1} = \omega_r\hat{a}^\dagger\hat{a} - \frac{\omega_r}{4\tilde{g}^4}(\hat{a}^\dagger + \hat{a})^2 - \frac{\omega_q}{4}(\tilde{g}^2 + \tilde{g}^{-2}). \tag{A6}$$

APPENDIX B: DIAGONALIZATION OF THE GENERAL SU(1,1) HAMILTONIAN

Equations (9) and (10) can be concluded into the general SU(1,1)-form Hamiltonian,

$$\hat{H} = c_1\hat{K}_0 + c_2(\hat{K}_+ + \hat{K}_-) + ic_3(\hat{K}_+ - \hat{K}_-) + c_4, \tag{B1}$$

where the coefficients c_1, c_2, c_3, c_4 are decided by the specific physical system. $\hat{K}_0 = (\hat{a}^\dagger\hat{a} + 1/2)/2$, $\hat{K}_+ = (\hat{a}^\dagger)^2/2$, $\hat{K}_- = \hat{a}^2/2$, and satisfy the commutation relations $[\hat{K}_0, \hat{K}_\pm] = \pm\hat{K}_\pm$, $[\hat{K}_+, \hat{K}_-] = -2\hat{K}_0$. $\hat{a}, \hat{a}^\dagger$ are the bosonic modes. The matrix form of Eq. (B1) reads

$$\hat{H} = \alpha^\dagger A\alpha + c_4, \tag{B2}$$

where

$$\alpha = \begin{pmatrix}\hat{a}\\ \hat{a}^\dagger\end{pmatrix} \quad A = \begin{pmatrix}\frac{c_1}{4} & \frac{c_2+ic_3}{2}\\ \frac{c_2-ic_3}{2} & \frac{c_1}{4}\end{pmatrix}. \tag{B3}$$

Equation (B2) can be diagonalized by the Bogoliubov-Valatin transformation with new bosonic modes

$$\beta = U\alpha, \tag{B4}$$

where

$$\beta = \begin{pmatrix}\hat{b}\\ \hat{b}^\dagger\end{pmatrix} \quad U = \begin{pmatrix}u & v\\ v^* & u^*\end{pmatrix}, \tag{B5}$$

with complex numbers u and v and $|u|^2 - |v|^2 = 1$. Accordingly, Eq. (B2) is written as

$$\begin{aligned}\hat{H} &= \alpha^\dagger U^\dagger(U^\dagger)^{-1}AU^{-1}U\alpha\\ &= \beta^\dagger(U^\dagger)^{-1}AU^{-1}\beta\\ &= \beta^\dagger\begin{pmatrix}\lambda_1 & 0\\ 0 & \lambda_2\end{pmatrix}\beta,\end{aligned} \tag{B6}$$

where the constant term c_4 is omitted. We then use the following hint to deduce the values of λ_1 and λ_2. Based on $|u|^2 - |v|^2 = 1$ one has $U\hat{\sigma}_zU^\dagger = \hat{\sigma}_z$ and $U = \hat{\sigma}_z(U^\dagger)^{-1}\hat{\sigma}_z$. Accordingly, we get

$$\begin{aligned}\hat{\sigma}_z(U^\dagger)^{-1}AU^{-1} &= \hat{\sigma}_z(U^\dagger)^{-1}\hat{\sigma}_z\hat{\sigma}_zAU^{-1}\\ = U\hat{\sigma}_zAU^{-1} &= \begin{pmatrix}\lambda_1 & 0\\ 0 & -\lambda_2\end{pmatrix}.\end{aligned} \tag{B7}$$

Inserting Eqs. (B3) and (B5) into (B7), we have

$$\lambda_1 = \lambda_2 = \frac{\sqrt{c_1^2 - 4c_2^2 - 4c_3^2}}{4}. \tag{B8}$$

For the Hamiltonian $\hat{H}_{np,\tilde{g}\leqslant 1}$ (9), its diagonized form is

$$\hat{H}_{np,\tilde{g}\leqslant 1} = \omega_r\sqrt{1 - \tilde{g}^2}\left(\hat{b}^\dagger\hat{b} + \frac{1}{2}\right) - \frac{\omega_q + \omega_r}{2}, \tag{B9}$$

where $c_1 = -\omega_r\tilde{g}^2 + 2\omega_r$, $c_2 = -\omega_r\tilde{g}^2/2$, $c_4 = \omega_q + \omega_r/2$. For the Hamiltonian $\hat{H}_{sp,\tilde{g}>1}$ (10), its diagonized form reads

$$\hat{H}_{sp,\tilde{g}>1} = \omega_r\sqrt{1-1/\tilde{g}^4}\left(\tilde{b}^{\dagger}\tilde{b} + \frac{1}{2}\right) - \frac{\omega_q(\tilde{g}^2 + \tilde{g}^{-2}) + 2\omega_r}{4}, \tag{B10}$$

where $c_1 = 2\omega_r - \omega_r/\tilde{g}^4$, $c_2 = -\omega_r/(2\tilde{g}^4)$, $c_4 = [-\omega_q(\tilde{g}^2 + \tilde{g}^{-2}) - 2\omega_r]/4$.

APPENDIX C: THE GENERATOR OF INFINITESIMAL VARIATIONS OF PARAMETER

The infinitesimal variations of $\tilde{g}$ with the general SU(1,1)-form Hamiltonian $\hat{H}(\tilde{g})$, are governed by its generator

$$\begin{aligned}
h_{\tilde{g}}(T) &= i(\partial_{\tilde{g}} e^{-i\hat{H}(\tilde{g})T})e^{i\hat{H}(\tilde{g})T}\\
&= i\int_0^1 ds e^{-i\hat{H}(\tilde{g})Ts}(-iT)\partial_{\tilde{g}}\hat{H}(\tilde{g})e^{-i\hat{H}(\tilde{g})T(1-s)}e^{i\hat{H}(\tilde{g})T}\\
&= T\int_0^1 ds e^{-i\hat{H}(\tilde{g})Ts}\partial_{\tilde{g}}\hat{H}(\tilde{g})e^{i\hat{H}(\tilde{g})Ts}\\
&= T\int_0^1 ds\left\{\partial_{\tilde{g}}\hat{H}(\tilde{g}) + [-i\hat{H}(\tilde{g})Ts, \partial_{\tilde{g}}\hat{H}(\tilde{g})] + \frac{1}{2!}[-i\hat{H}(\tilde{g})Ts, [-i\hat{H}(\tilde{g})Ts, \partial_{\tilde{g}}\hat{H}(\tilde{g})]] + \cdots\right\}\\
&= i\sum_{n=0}^{\infty}\frac{(-iT)^{n+1}}{(n+1)!}\hat{H}(\tilde{g})^{\times n}[\partial_{\tilde{g}}\hat{H}(\tilde{g})],
\end{aligned} \tag{C1}$$

where the notation $\hat{A}^{\times n}(\bullet) := \overbrace{[\hat{A}, [\hat{A}, \cdots [\hat{A},}^{n\text{ times}} \bullet]$ is introduced to express the nested commutators. In the above calculations, the derivative of an exponential operator $\partial_\ell e^{\hat{A}} = \int_0^1 ds\ e^{s\hat{A}}(\partial_\ell\hat{A})e^{(1-s)\hat{A}}$ and the well-known expansion $e^{\hat{A}}\hat{B}e^{-\hat{A}} = \hat{B} + [\hat{A}, \hat{B}] + (1/2!)[\hat{A}, [\hat{A}, \hat{B}]] + \cdots$ are employed [44].

From Eq. (B1) we get

$$\begin{aligned}
\partial_{\tilde{g}}\hat{H} &= \partial_{\tilde{g}}c_1\hat{K}_0 + \partial_{\tilde{g}}c_2(\hat{K}_+ + \hat{K}_-) + \partial_{\tilde{g}}c_4,\\
\hat{H}^{\times 1}(\partial_{\tilde{g}}\hat{H}) &= (c_1\partial_{\tilde{g}}c_2 - c_2\partial_{\tilde{g}}c_1)(\hat{K}_+ - \hat{K}_-),\\
\hat{H}^{\times 3}(\partial_{\tilde{g}}\hat{H}) &= \left(c_1^2 - 4c_2^2\right)(c_1\partial_{\tilde{g}}c_2 - c_2\partial_{\tilde{g}}c_1)(\hat{K}_+ - \hat{K}_-),\\
\hat{H}^{\times 5}(\partial_{\tilde{g}}\hat{H}) &= \left(c_1^2 - 4c_2^2\right)^2(c_1\partial_{\tilde{g}}c_2 - c_2\partial_{\tilde{g}}c_1)(\hat{K}_+ - \hat{K}_-),\\
&\cdots\\
\hat{H}^{\times 2}(\partial_{\tilde{g}}\hat{H}) &= (c_1\partial_{\tilde{g}}c_2 - c_2\partial_{\tilde{g}}c_1)[c_1(\hat{K}_+ + \hat{K}_-) + 4c_2\hat{K}_0],\\
\hat{H}^{\times 4}(\partial_{\tilde{g}}\hat{H}) &= \left(c_1^2 - 4c_2^2\right)(c_1\partial_{\tilde{g}}c_2 - c_2\partial_{\tilde{g}}c_1)[c_1(\hat{K}_+ + \hat{K}_-) + 4c_2\hat{K}_0],\\
\hat{H}^{\times 6}(\partial_{\tilde{g}}\hat{H}) &= \left(c_1^2 - 4c_2^2\right)^2(c_1\partial_{\tilde{g}}c_2 - c_2\partial_{\tilde{g}}c_1)[c_1(\hat{K}_+ + \hat{K}_-) + 4c_2\hat{K}_0],\\
&\cdots
\end{aligned} \tag{C2}$$

where $c_3 = 0$ is set for simplification. Inserting Eq. (C2) into Eq. (C1), we get

$$\begin{aligned}
h_{\tilde{g}}(T) =& T\partial_{\tilde{g}}\hat{H} - i\frac{T^2}{2!}\hat{H}^{\times 1}(\partial_{\tilde{g}}\hat{H}) - \frac{T^3}{3!}\hat{H}^{\times 2}(\partial_{\tilde{g}}\hat{H}) + i\frac{T^4}{4!}\hat{H}^{\times 3}(\partial_{\tilde{g}}\hat{H})\\
&+ \frac{T^5}{5!}\hat{H}^{\times 4}(\partial_{\tilde{g}}\hat{H}) - i\frac{T^6}{6!}\hat{H}^{\times 5}(\partial_{\tilde{g}}\hat{H}) - \frac{T^7}{7!}\hat{H}^{\times 6}(\partial_{\tilde{g}}\hat{H}) + \cdots\\
=& T\partial_{\tilde{g}}\hat{H} - \left[\frac{T^3}{3!}\hat{H}^{\times 2}(\partial_{\tilde{g}}\hat{H}) - \frac{T^5}{5!}\hat{H}^{\times 4}(\partial_{\tilde{g}}\hat{H}) + \frac{T^7}{7!}\hat{H}^{\times 6}(\partial_{\tilde{g}}\hat{H}) + \cdots\right]\\
&- i\left[\frac{T^2}{2!}\hat{H}^{\times 1}(\partial_{\tilde{g}}\hat{H}) - \frac{T^4}{4!}\hat{H}^{\times 3}(\partial_{\tilde{g}}\hat{H}) + \frac{T^6}{6!}\hat{H}^{\times 5}(\partial_{\tilde{g}}\hat{H}) + \cdots\right]\\
=& T[\partial_{\tilde{g}}c_1\hat{K}_0 + \partial_{\tilde{g}}c_2(\hat{K}_+ + \hat{K}_-) + \partial_{\tilde{g}}c_4]\\
&- (c_1\partial_{\tilde{g}}c_2 - c_2\partial_{\tilde{g}}c_1)[c_1(\hat{K}_+ + \hat{K}_-) + 4c_2K_0]\left[\frac{T^3}{3!} - \frac{T^5}{5!}\left(c_1^2 - 4c_2^2\right) + \frac{T^7}{7!}\left(c_1^2 - 4c_2^2\right)^2 + \cdots\right]
\end{aligned}$$

$$\begin{aligned}
&-i(c_1\partial_{\tilde g}c_2-c_2\partial_{\tilde g}c_1)(\hat K_+-\hat K_-)\left[\frac{T^2}{2!}-\frac{T^4}{4!}\left(c_1^2-4c_2^2\right)+\frac{T^6}{6!}(c_1^2-4c_2)^2+\cdots\right]\\
=\,&T[\partial_{\tilde g}c_1\hat K_0+\partial_{\tilde g}c_2(\hat K_++\hat K_-)+\partial_{\tilde g}c_4]\\
&-\frac{(c_1\partial_{\tilde g}c_2-c_2\partial_{\tilde g}c_1)}{\left(c_1^2-4c_2^2\right)^{3/2}}[c_1(\hat K_++\hat K_-)+4c_2\hat K_0]\left[\frac{T^3}{3!}\left(c_1^2-4c_2^2\right)^{3/2}-\frac{T^5}{5!}\left(c_1^2-4c_2^2\right)^{5/2}+\frac{T^7}{7!}\left(c_1^2-4c_2^2\right)^{7/2}+\cdots\right]\\
&-i\frac{(c_1\partial_{\tilde g}c_2-c_2\partial_{\tilde g}c_1)}{c_1^2-4c_2^2}(\hat K_+-\hat K_-)\left[\frac{T^2}{2!}\left(c_1^2-4c_2^2\right)^{2/2}-\frac{T^4}{4!}\left(c_1^2-4c_2^2\right)^{4/2}+\frac{T^6}{6!}\left(c_1^2-4c_2^2\right)^{6/2}+\cdots\right]\\
=\,&T[\partial_{\tilde g}c_1\hat K_0+\partial_{\tilde g}c_2(\hat K_++\hat K_-)+\partial_{\tilde g}c_4]\\
&+\frac{(c_1\partial_{\tilde g}c_2-c_2\partial_{\tilde g}c_1)}{\left(c_1^2-4c_2^2\right)^{3/2}}[c_1(\hat K_++\hat K_-)+4c_2\hat K_0]\left[\sin\left(T\sqrt{c_1^2-4c_2^2}\right)-T\sqrt{c_1^2-4c_2^2}\right]\\
&+i\frac{(c_1\partial_{\tilde g}c_2-c_2\partial_{\tilde g}c_1)}{c_1^2-4c_2^2}(\hat K_+-\hat K_-)\left[\cos\left(T\sqrt{c_1^2-4c_2^2}\right)-1\right]\\
=&\left\{T\partial_{\tilde g}c_1+\frac{4c_2(c_1\partial_{\tilde g}c_2-c_2\partial_{\tilde g}c_1)}{\left(c_1^2-4c_2^2\right)^{3/2}}\left[\sin\left(T\sqrt{c_1^2-4c_2^2}\right)-T\sqrt{c_1^2-4c_2^2}\right]\right\}\hat K_0\\
&+\left\{T\partial_{\tilde g}c_2+\frac{c_1(c_1\partial_{\tilde g}c_2-c_2\partial_{\tilde g}c_1)}{\left(c_1^2-4c_2^2\right)^{3/2}}\left[\sin\left(T\sqrt{c_1^2-4c_2^2}\right)-T\sqrt{c_1^2-4c_2^2}\right]\right\}(\hat K_++\hat K_-)\\
&+i\frac{(c_1\partial_{\tilde g}c_2-c_2\partial_{\tilde g}c_1)}{c_1^2-4c_2^2}\left[\cos\left(T\sqrt{c_1^2-4c_2^2}\right)-1\right](\hat K_+-\hat K_-)+T\partial_{\tilde g}c_4.
\end{aligned}\tag{C3}$$

For the $\hat H_{np,\tilde g\leqslant 1}$ (9), $c_1=-\omega_r\tilde g^2+2\omega_r$, $c_2=-\frac{\omega_r\tilde g^2}{2}$, $c_4=-\frac{\omega_q+\omega_r}{2}$, from Eq. (C3) we get

$$h_{\tilde g\leqslant 1}(T)=f_x\hat K_0+f_y(\hat K_++\hat K_-)+if_z(\hat K_+-\hat K_-),\tag{C4}$$

with

$$\begin{aligned}
f_x&=-2\tilde gT\omega_r+\frac{\tilde g^3}{2(1-\tilde g^2)^{3/2}}[\sin(2T\omega_r\sqrt{1-\tilde g^2})-2T\omega_r\sqrt{1-\tilde g^2}],\\
f_y&=-\tilde gT\omega_r+\frac{-2\tilde g+\tilde g^3}{4(1-\tilde g^2)^{3/2}}[\sin(2T\omega_r\sqrt{1-\tilde g^2})-2T\omega_r\sqrt{1-\tilde g^2}],\\
f_z&=\frac{\tilde g}{2(\tilde g^2-1)}[\cos(2T\omega_r\sqrt{1-\tilde g^2})-1].
\end{aligned}\tag{C5}$$

For the $\hat H_{sp,\tilde g>1}$ (10), $c_1=2\omega_r-\frac{\omega_r}{\tilde g^4}$, $c_2=-\frac{\omega_r}{2\tilde g^4}$, $c_4=-\frac{\omega_q(\tilde g^2+\tilde g^{-2})+2\omega_r}{4}$, from Eq. (C3) we get

$$h_{\tilde g>1}(T)=\tilde f_x\hat K_0+\tilde f_y(\hat K_++\hat K_-)+i\tilde f_z(\hat K_+-\hat K_-)+\tilde f_h,\tag{C6}$$

with

$$\begin{aligned}
\tilde f_x&=\frac{4T\omega_r}{\tilde g^5}-\frac{1}{\tilde g^9(1-1/\tilde g^4)^{3/2}}\left[\sin\left(\frac{T}{\tilde g^2}\sqrt{2\omega_r+\omega_r^2(2\tilde g^2-1/\tilde g^2)^2}\right)-\frac{T}{\tilde g^2}\sqrt{2\omega_r+\omega_r^2(2\tilde g^2-1/\tilde g^2)^2}\right],\\
\tilde f_y&=\frac{2T\omega_r}{\tilde g^5}+\frac{2\tilde g^4-1}{2\tilde g^9(1-1/\tilde g^4)^{3/2}}\left[\sin\left(\frac{T}{\tilde g^2}\sqrt{2\omega_r+\omega_r^2(2\tilde g^2-1/\tilde g^2)^2}\right)-\frac{T}{\tilde g^2}\sqrt{2\omega_r+\omega_r^2(2\tilde g^2-1/\tilde g^2)^2}\right],\\
\tilde f_z&=\frac{-1}{\tilde g-\tilde g^5}\left[\cos\left(\frac{T}{\tilde g^2}\sqrt{2\omega_r+\omega_r^2(2\tilde g^2-1/\tilde g^2)^2}\right)-1\right],\quad \tilde f_h=\frac{-T\omega_q(\tilde g^4-1)}{2\tilde g^3}.
\end{aligned}\tag{C7}$$

The QFI of parameter $\xi\in\{\Omega_0,\omega_q,m\}$ encoded in $\tilde g$ can be expressed as

$$I_\xi(T)=4\mathrm{Var}[h_\xi(T)]_{|\psi_0\rangle},\tag{C8}$$

where $h_\xi(T)$ is the generator of infinitesimal variations of ξ,

$$\begin{aligned} h_\xi(T) &= i(\partial_\xi e^{-i\hat{H}(\tilde{g})T})e^{i\hat{H}(\tilde{g})T} \\ &= i\sum_{n=0}^{\infty}\frac{(-iT)^{n+1}}{(n+1)!}\hat{H}(\tilde{g})^{\times n}[\partial_\xi \hat{H}(\tilde{g})] \\ &= i\sum_{n=0}^{\infty}\frac{(-iT)^{n+1}}{(n+1)!}\hat{H}(\tilde{g})^{\times n}[\partial_{\tilde{g}}\hat{H}(\tilde{g})(\partial_\xi \tilde{g}) + C_0(\xi)] \\ &= (\partial_\xi \tilde{g})h_{\tilde{g}}(T) + C_0(\xi)T. \end{aligned} \tag{C9}$$

In the third line of the above equation, we have assumed that the condition $\partial_\xi \hat{H}(\tilde{g}) = \partial_{\tilde{g}}\hat{H}(\tilde{g})(\partial_\xi \tilde{g}) + C_0(\xi)$ is satisfied, where $C_0(\xi)$ is a function of ξ. Note that the term of C_0 vanishes in the higher commutation terms and can be eliminated in the variance of $h_\xi(T)$.

Then $I_\xi(T)$ can be rewritten as

$$\begin{aligned} I_\xi(T) &= 4[\langle h_\xi(T)^2\rangle - \langle h_\xi(T)\rangle^2] \\ &= 4(\partial_\xi \tilde{g})^2[\langle h_{\tilde{g}}(T)^2\rangle - \langle h_{\tilde{g}}(T)\rangle^2] \\ &= (\partial_\xi \tilde{g})^2 I_{\tilde{g}}(T). \end{aligned} \tag{C10}$$

APPENDIX D: THE AVERAGE PHONON NUMBER

The average phonon number during the dynamic evolution, denoted by $\langle\hat{N}\rangle$ in Eq. (38) can be computed using the Heisenberg equations of motion, as shown in Eqs. (39)–(41). For the initial superposition state $(|0\rangle + i|n\rangle)/\sqrt{2}$,

$$\langle\hat{N}\rangle = \frac{(n+1)[(\tilde{g}^2-2)^2 - \tilde{g}^4\cos(2\sqrt{1-\tilde{g}^2}\omega_r T)]}{8(1-\tilde{g}^2)} - \frac{1}{2}, \tag{D1}$$

with the limitation of average phonon number $\langle\hat{N}\rangle_{\tilde{g}_c} = [2n + (1+n)\omega_r^2 T^2]/4$ at the critical point $\tilde{g} = \tilde{g}_c = 1$, and the maximum of average phonon number during the evolution $\langle\hat{N}\rangle_{\max} = n/2 + (n+1)\tilde{g}^4/(4-4\tilde{g}^2)$.

For the Fock state $|n\rangle$,

$$\langle\hat{N}\rangle = \frac{(2n+1)[(\tilde{g}^2-2)^2 - \tilde{g}^4\cos(2\sqrt{1-\tilde{g}^2}\omega_r T)]}{8(1-\tilde{g}^2)} - \frac{1}{2}, \tag{D2}$$

with the limitation of average phonon number $\langle\hat{N}\rangle_{\tilde{g}_c} = [4n + (1+2n)\omega_r^2 T^2]/4$ at the critical point $\tilde{g} = \tilde{g}_c = 1$, the maximum of average phonon number during the evolution $\langle\hat{N}\rangle_{\max} = n + (2n+1)\tilde{g}^4/(4-4\tilde{g}^2)$.

For the coherent initial state $a|\alpha\rangle = \alpha|\alpha\rangle$ with $\alpha = \mathrm{Re}[\alpha] + i\mathrm{Im}[\alpha]$,

$$\begin{aligned} \langle\hat{N}\rangle = \frac{1}{8(1-\tilde{g}^2)}\{ & 8(\mathrm{Re}[\alpha]^2 + \mathrm{Im}[\alpha]^2) + (4\mathrm{Re}[\alpha]^2 + 1)\tilde{g}^4 \\ & - 4\tilde{g}^2(3\mathrm{Re}[\alpha]^2 + \mathrm{Im}[\alpha]^2) \\ & + \tilde{g}^2[(4\mathrm{Re}[\alpha]^2 - 4\mathrm{Im}[\alpha]^2 - 4\mathrm{Re}[\alpha]^2\tilde{g}^2 - \tilde{g}^2) \\ & \times \cos(2\sqrt{1-\tilde{g}^2}\omega_r T) \\ & - 8\mathrm{Re}[\alpha]\mathrm{Im}[\alpha]\sqrt{1-\tilde{g}^2}\sin(2\sqrt{1-\tilde{g}^2}\omega_r T)]\}, \end{aligned} \tag{D3}$$

with the limitation of average phonon number $\langle\hat{N}\rangle_{\tilde{g}_c} = \mathrm{Re}[\alpha]^2 + \mathrm{Im}[\alpha]^2 - 2\mathrm{Re}[\alpha]\mathrm{Im}[\alpha]\omega_r T + (1 + 4\mathrm{Im}[\alpha]^2)\omega_r^2 T^2$ at the critical point $\tilde{g} = \tilde{g}_c = 1$. One should examine various scenarios regarding the maximum average phonon number during the evolution with different α values. $\langle\hat{N}\rangle_{\max} = (\tilde{g}^4 + 4\mathrm{Im}[\alpha]^2)/(4-4\tilde{g}^2)$ for $\mathrm{Re}[\alpha] = 0$. When $\mathrm{Im}[\alpha] = 0$ and $\mathrm{Re}[\alpha] < \tilde{g}/(2\sqrt{1-\tilde{g}^2})$, $\langle\hat{N}\rangle_{\max} = \mathrm{Re}[\alpha]^2$. When $\mathrm{Im}[\alpha] = 0$ and $\mathrm{Re}[\alpha] > \tilde{g}/(2\sqrt{1-\tilde{g}^2})$, $\langle\hat{N}\rangle_{\max} = \mathrm{Re}[\alpha]^2(1-\tilde{g}^2) + \tilde{g}^4/(4-4\tilde{g}^2)$.

---

[1] C. L. Degen, F. Reinhard, and P. Cappellaro, Quantum sensing, Rev. Mod. Phys. **89**, 035002 (2017).

[2] H. Yuan and C.-H. F. Fung, Optimal feedback scheme and universal time scaling for Hamiltonian parameter estimation, Phys. Rev. Lett. **115**, 110401 (2015).

[3] H. Yuan, Sequential feedback scheme outperforms the parallel scheme for Hamiltonian parameter estimation, Phys. Rev. Lett. **117**, 160801 (2016).

[4] S. Pang and A. N. Jordan, Optimal adaptive control for quantum metrology with time-dependent Hamiltonians, Nat. Commun. **8**, 14695 (2017).

[5] Z. Hou, J.-F. Tang, H. Chen, H. Yuan, G.-Y. Xiang, C.-F. Li, and G.-C. Guo, Zero–trade-off multiparameter quantum estimation via simultaneously saturating multiple Heisenberg uncertainty relations, Sci. Adv. **7**, eabd2986 (2021).

[6] X. Zhao, Y. Yang, and G. Chiribella, Quantum metrology with indefinite causal order, Phys. Rev. Lett. **124**, 190503 (2020).

[7] P. Yin, X. Zhao, Y. Yang, Y. Guo, W.-H. Zhang, G.-C. Li, Y.-J. Han, B.-H. Liu, J.-S. Xu, G. Chiribella *et al.*, Experimental super-Heisenberg quantum metrology with indefinite gate order, Nat. Phys. **19**, 1122 (2023).

[8] S. Fernández-Lorenzo and D. Porras, Quantum sensing close to a dissipative phase transition: Symmetry breaking and criticality as metrological resources, Phys. Rev. A **96**, 013817 (2017).

[9] R. Di Candia, F. Minganti, K. Petrovnin, G. Paraoanu, and S. Felicetti, Critical parametric quantum sensing, npj Quantum Inf. **9**, 23 (2023).

[10] R. Salvia, M. Mehboudi, and M. Perarnau-Llobet, Critical quantum metrology assisted by real-time feedback control, Phys. Rev. Lett. **130**, 240803 (2023).

[11] C. Hotter, H. Ritsch, and K. Gietka, Combining critical and quantum metrology, Phys. Rev. Lett. **132**, 060801 (2024).

[12] X.-W. Luo, C. Zhang, and S. Du, Quantum squeezing and sensing with pseudo-anti-parity-time symmetry, Phys. Rev. Lett. **128**, 173602 (2022).

[13] W. Ding, X. Wang, and S. Chen, Fundamental sensitivity limits for non-Hermitian quantum sensors, Phys. Rev. Lett. **131**, 160801 (2023).

[14] J. Naikoo, R. W. Chhajlany, and J. Kołodyński, Multiparameter estimation perspective on non-Hermitian singularity-enhanced sensing, Phys. Rev. Lett. **131**, 220801 (2023).

[15] M. Yu, X. Li, Y. Chu, B. Mera, F. N. Ünal, P. Yang, Y. Liu, N. Goldman, and J. Cai, Experimental demonstration of topological bounds in quantum metrology, Natl. Sci. Rev. **11**, nwae065 (2024).

[16] Y. Yang, H. Yuan, and F. Li, Quantum multiparameter estimation enhanced by a topological phase transition, Phys. Rev. A **109**, 022604 (2024).

[17] S. Gammelmark and K. Mølmer, Phase transitions and Heisenberg limited metrology in an Ising chain interacting with a single-mode cavity field, New J. Phys. **13**, 053035 (2011).

[18] D.-S. Ding, Z.-K. Liu, B.-S. Shi, G.-C. Guo, K. Mølmer, and C. S. Adams, Enhanced metrology at the critical point of a many-body Rydberg atomic system, Nat. Phys. **18**, 1447 (2022).

[19] A. Carollo, D. Valenti, and B. Spagnolo, Geometry of quantum phase transitions, Phys. Rep. **838**, 1 (2020).

[20] M.-J. Hwang, R. Puebla, and M. B. Plenio, Quantum phase transition and universal dynamics in the Rabi model, Phys. Rev. Lett. **115**, 180404 (2015).

[21] L. Garbe, M. Bina, A. Keller, M. G. A. Paris, and S. Felicetti, Critical quantum metrology with a finite-component quantum phase transition, Phys. Rev. Lett. **124**, 120504 (2020).

[22] K. Gietka, F. Metz, T. Keller, and J. Li, Adiabatic critical quantum metrology cannot reach the Heisenberg limit even when shortcuts to adiabaticity are applied, Quantum **5**, 489 (2021).

[23] Y. Chu, S. Zhang, B. Yu, and J. Cai, Dynamic framework for criticality-enhanced quantum sensing, Phys. Rev. Lett. **126**, 010502 (2021).

[24] J.-H. Lü, W. Ning, X. Zhu, F. Wu, L.-T. Shen, Z.-B. Yang, and S.-B. Zheng, Critical quantum sensing based on the Jaynes-Cummings model with a squeezing drive, Phys. Rev. A **106**, 062616 (2022).

[25] S.-B. Tang, H. Qin, B.-B. Liu, D.-Y. Wang, K. Cui, S.-L. Su, L.-L. Yan, and G. Chen, Enhancement of quantum sensing in a cavity-optomechanical system around the quantum critical point, Phys. Rev. A **108**, 053514 (2023).

[26] D. Leibfried, R. Blatt, C. Monroe, and D. Wineland, Quantum dynamics of single trapped ions, Rev. Mod. Phys. **75**, 281 (2003).

[27] R. Blatt and C. F. Roos, Quantum simulations with trapped ions, Nat. Phys. **8**, 277 (2012).

[28] A. C. Wilson, Y. Colombe, K. R. Brown, E. Knill, D. Leibfried, and D. J. Wineland, Tunable spin–spin interactions and entanglement of ions in separate potential wells, Nature (London) **512**, 57 (2014).

[29] R. Srinivas, S. C. Burd, R. T. Sutherland, A. C. Wilson, D. J. Wineland, D. Leibfried, D. T. C. Allcock, and D. H. Slichter, Trapped-ion spin-motion coupling with microwaves and a near-motional oscillating magnetic field gradient, Phys. Rev. Lett. **122**, 163201 (2019).

[30] D. M. Meekhof, C. Monroe, B. E. King, W. M. Itano, and D. J. Wineland, Generation of nonclassical motional states of a trapped atom, Phys. Rev. Lett. **76**, 1796 (1996).

[31] C.-w. Chou, C. Kurz, D. B. Hume, P. N. Plessow, D. R. Leibrandt, and D. Leibfried, Preparation and coherent manipulation of pure quantum states of a single molecular ion, Nature (London) **545**, 203 (2017).

[32] S. Colombo, E. Pedrozo-Peñafiel, A. F. Adiyatullin, Z. Li, E. Mendez, C. Shu, and V. Vuletić, Time-reversal-based quantum metrology with many-body entangled states, Nat. Phys. **18**, 925 (2022).

[33] K. C. McCormick, J. Keller, S. C. Burd, D. J. Wineland, A. C. Wilson, and D. Leibfried, Quantum-enhanced sensing of a single-ion mechanical oscillator, Nature (London) **572**, 86 (2019).

[34] K. A. Gilmore, M. Affolter, R. J. Lewis-Swan, D. Barberena, E. Jordan, A. M. Rey, and J. J. Bollinger, Quantum-enhanced sensing of displacements and electric fields with two-dimensional trapped-ion crystals, Science **373**, 673 (2021).

[35] M.-L. Cai, Z.-D. Liu, W.-D. Zhao, Y.-K. Wu, Q.-X. Mei, Y. Jiang, L. He, X. Zhang, Z.-C. Zhou, and L.-M. Duan, Observation of a quantum phase transition in the quantum Rabi model with a single trapped ion, Nat. Commun. **12**, 1126 (2021).

[36] J. Pedernales, I. Lizuain, S. Felicetti, G. Romero, L. Lamata, and E. Solano, Quantum Rabi model with trapped ions, Sci. Rep. **5**, 15472 (2015).

[37] R. Puebla, M.-J. Hwang, J. Casanova, and M. B. Plenio, Probing the dynamics of a superradiant quantum phase transition with a single trapped ion, Phys. Rev. Lett. **118**, 073001 (2017).

[38] D. Lv, S. An, Z. Liu, J.-N. Zhang, J. S. Pedernales, L. Lamata, E. Solano, and K. Kim, Quantum simulation of the quantum Rabi model in a trapped ion, Phys. Rev. X **8**, 021027 (2018).

[39] J. Larson and E. K. Irish, Some remarks on 'superradiant' phase transitions in light-matter systems, J. Phys. A: Math. Theor. **50**, 174002 (2017).

[40] Y.-Z. Lai, J.-Q. Liang, H. J. W. Müller-Kirsten, and J.-G. Zhou, Time-dependent quantum systems and the invariant Hermitian operator, Phys. Rev. A **53**, 3691 (1996).

[41] S. L. Braunstein and C. M. Caves, Statistical distance and the geometry of quantum states, Phys. Rev. Lett. **72**, 3439 (1994).

[42] E. Polino, M. Valeri, N. Spagnolo, and F. Sciarrino, Photonic quantum metrology, AVS Quantum Sci. **2**, 024703 (2020).

[43] V. Giovannetti, S. Lloyd, and L. Maccone, Quantum metrology, Phys. Rev. Lett. **96**, 010401 (2006).

[44] R. M. Wilcox, Exponential operators and parameter differentiation in quantum physics, J. Math. Phys. **8**, 962 (1967).

[45] A. Zavatta, S. Viciani, and M. Bellini, Quantum-to-classical transition with single-photon-added coherent states of light, Science **306**, 660 (2004).

[46] H. M. Wiseman and G. J. Milburn, *Quantum Measurement and Control* (Cambridge University Press, Cambridge, 2009).

[47] J. F. Barry, J. M. Schloss, E. Bauch, M. J. Turner, C. A. Hart, L. M. Pham, and R. L. Walsworth, Sensitivity optimization for NV-diamond magnetometry, Rev. Mod. Phys. **92**, 015004 (2020).

[48] M.-J. Hwang, P. Rabl, and M. B. Plenio, Dissipative phase transition in the open quantum Rabi model, Phys. Rev. A **97**, 013825 (2018).

[49] W. Ge, K. Jacobs, S. Asiri, M. Foss-Feig, and M. S. Zubairy, Operational resource theory of nonclassicality via quantum metrology, Phys. Rev. Res. **2**, 023400 (2020).

[50] N. Akhtar, J. Wu, J.-X. Peng, W.-M. Liu, and G. Xianlong, Sub-Planck structures and sensitivity of the superposed photon-added or photon-subtracted squeezed-vacuum states, Phys. Rev. A **107**, 052614 (2023).